

Uncovering the synergy between gold and sodium on ZrO₂ for boosting the reverse water gas shift reaction: *In-situ* spectroscopic investigations

Abdallah I.M. Rabee^{a,b,*}, Sebastian Cisneros^a, Dan Zhao^a, Carsten R. Kreyenschulte^a,
Stephan Bartling^a, Vita Kondratenko^a, Christoph Kubis^a, Evgenii V. Kondratenko^a,
Angelika Brückner^{a,c}, Jabor Rabeah^{a,*}

^a Leibniz-Institut für Katalyse, Albert-Einstein-Str. 29A, 18059 Rostock, Germany

^b Chemistry Department, Faculty of Science, Minia University, El-Minia 61519, Egypt

^c Department Life, Light and Matter, University of Rostock, Albert-Einstein-Str. 25, 18059 Rostock, Germany

ARTICLE INFO

Keywords:

Reverse water–gas shift
CO₂ hydrogenation
Gold catalyst
In-situ spectroscopy
Oxygen vacancy

ABSTRACT

CO₂ conversion to CO via the reverse water-gas shift (RWGS) reaction is a promising source of syngas for subsequent synthesis of liquid fuels and chemicals. Herein, we present the synthesis of catalysts containing Au supported on hydroxylated Na-modified ZrO₂, with Au amounts ranging from 0.05 to 1 wt%. Systematic investigations reveal the formation of cooperative Au/Na sites at the interface. These sites cooperate synergistically to activate CO₂ and generate a high surface density of carboxylate-like species, which serve as highly active intermediates for CO formation. It was found that the RWGS reaction on the catalyst with low Au loading proceeds mainly via a carboxylate pathway, with bidentate formate acting as spectators. At higher Au loading, the bidentate formate pathway contributes somewhat to CO formation alongside the carboxylate pathway. Based on temporal analysis of products, we emphasize the significant roles of H₂ spillover and the metal-support interface in the RWGS reaction.

1. Introduction

Carbon dioxide (CO₂) emissions are a global concern due to their contribution to the greenhouse effect [1,2]. The reverse water-gas shift (RWGS) reaction has recently received significant attention as a promising method for converting CO₂ into CO, which can subsequently be transformed into valuable chemicals [1,3]. The rational design of highly efficient catalysts for RWGS requires a thorough understanding of the reaction mechanism. Although, considerable progress has been made in this regard with the assistance of *in situ* spectroscopic techniques [1,4], there are still controversial discussions. The associative (formate) and redox pathways have been extensively discussed in the literature as potential reaction mechanisms for the RWGS reaction [1,4]. According to computational studies by Mavrikakis et al. [5,6], carboxyl (COOH) species were also identified as key intermediates in the water-gas shift (WGS) reaction. Since then, the COOH-mediated pathway has been suggested as an energetically favorable route for the RWGS in both experimental and theoretical studies [4]. However, experimental

evidence supporting the existence of these species still remains a matter of debate [7].

Various oxides, including TiO₂ [8–11], ZrO₂ [8,11], Fe₂O₃ [8], CeO₂ [8,12,13], and Al₂O₃ [10], have been reported as supports for the RWGS reaction, with higher activity observed over reducible supports. Our recent study demonstrated that low-loaded Au/ZrO₂ catalysts exhibit RWGS activity, albeit with lower activity than Au/TiO₂ [11]. Nonetheless, ZrO₂ offers several advantages, including high thermal stability and superior mechanical properties, [14] which play a pivotal role in sustaining catalyst stability and enhancing heat and mass transfer. Moreover, ZrO₂ exhibits redox properties and exposes both acidic and basic sites, crucial for CO₂ adsorption and activation [15,16]. Furthermore, ZrO₂ demonstrates a higher capability to disperse Au [11]. These collective attributes render it an ideal support in various catalytic applications. With these properties in mind, we decided to reexamine ZrO₂-supported Au catalysts, aiming to enhance their RWGS activity.

Flytzani-Stephanopoulos et al. [17,18] studied the WGS over Pt and Au catalysts. They found that Au and Pt catalysts supported on

* Corresponding author at: Leibniz-Institut für Katalyse, Albert-Einstein-Str. 29A, 18059 Rostock, Germany.

* Corresponding author.

E-mail addresses: Abdallah.Ahmed@catalysis.de (A.I.M. Rabee), Jabor.Rabeah@catalysis.de (J. Rabeah).

<https://doi.org/10.1016/j.apcatb.2023.123685>

Received 24 October 2023; Received in revised form 15 December 2023; Accepted 30 December 2023

Available online 3 January 2024

0926-3373/© 2024 Elsevier B.V. All rights reserved.

alkali-modified, irreducible, and earth-abundant oxides such as alumina and silica-based supports, exhibited intrinsic activity comparable to that observed on reducible supports like CeO_x , FeO_x , and TiO_x . They attributed this promotion to the formation of common active sites on all supports, regardless of their reducibility, consisting of (Au or Pt)-OH_x-O-(Na or K) ensembles [17,18]. Alkali metal have also been reported as promoters for the RWGS reaction [19–21]. Morse et al. [19] found that Na and K species act as structural and electronic promoters for tungsten carbide, improving CO_2 adsorption. Odriozola et al. [20] showed that the promotional effect of Na on Pt-containing catalysts mainly arises from altering the electronic structure of Pt particles, creating new sites that favor CO_2 dissociation. Another study by Odriozola et al., [22], showed a significant role for Na in increasing CO_2 hydrogenation to CH_4 over $\text{Ru}/\text{Al}_2\text{O}_3$ by modifying the surface intermediate. They reported that the presence of Na inhibits the formation of bicarbonate and, thus, the subsequent hydrogenation to formate, leading to a change in the reaction mechanism from the formate pathway to the formyl pathway. However, despite these findings, the precise role of alkali addition in the reaction pathway and its control of the reaction intermediates remain unclear.

Therefore, this study is designed to develop highly active and selective Au catalysts for the RWGS reaction, with a particular emphasis on unraveling the role of Na ions and identifying the active intermediates responsible for CO formation. Our approach involves fine-tuning the surface properties of ZrO_2 with alkali metals to tailor the reaction intermediates and optimize their interaction with the support. Previous research has shown that the surface properties of ZrO_2 can be controlled by adjusting the pH during precipitation [23,24]. During the preparation of ZrO_2 , continuous condensation reactions tend to reduce the number of available reactive Zr-OH groups. However, when zirconium hydroxide is prepared at a higher pH (>10) using NaOH, some of the Zr-OH groups transform into Zr-O-Na linkages, which prevent their participation in condensation reactions [25]. Consequently, ZrO_2 surfaces prepared with an excess of NaOH predominantly exhibit (-O-Na) linkages [25,26]. Based on the aforementioned literature, these Na species are expected to play a significant role, along with Au, in boosting the RWGS reaction. To accomplish the objectives of this study, ZrO_2 with surface -O-Na was initially prepared using the precipitation method at a high pH (≥ 12) and subsequently employed as a support for Au catalysts. The catalysts were then investigated in-depth by a variety of techniques, including *ex-situ* and *in-situ* methods.

2. Experimental section

2.1. Material and catalyst preparation

ZrO_2 was synthesized by precipitation in aqueous solution at 25 °C. 1 M NaOH (99.1%, Fisher Chemical) was added dropwise to 200 ml of 0.1 M $\text{ZrOCl}_2 \cdot 8\text{H}_2\text{O}$ (99.9%, Alfa Aesar) under stirring till pH = 12.5. The precipitate was left for 20 h in contact with the mother liquor and then filtered, washed with distilled water, and dried at 100 °C for 12 h. The dried material was ground and calcined at 500 °C (at 2 °C/min) for 3 h under synthetic air flow.

Au catalysts with a nominal Au loading between 0.05 and 1 wt% were prepared by a deposition–precipitation method. Typically, 1.0 g of the ZrO_2 powder were added to 20 ml of an aqueous solution of HAuCl_4 (99.995%, Sigma-Aldrich). It's worth noting that the pH value, when 1.0 g of bare ZrO_2 was dissolved in 20 ml of deionized water, was 10.7. In contrast, the pH values when 1.0 g of bare ZrO_2 was added to a solution of HAuCl_4 to prepare catalysts with nominal Au loadings of 0.05, 0.10, 0.5, and 1 wt% were 10.4, 10.1, 9.7, and 9.3, respectively. Therefore, to maintain a constant pH for the preparation of all catalysts, we decided to set the pH at 11 by adding 0.1 M NaOH dropwise, which was an appropriate value for all the catalysts. After that, the suspensions were stirred at 25 °C for 3 h, filtered and washed thoroughly with deionized water. Finally, the samples were dried at 80 °C for 12 h, and

then used without any further heat treatment. The obtained Au catalysts are designated x AuZr, where x stands for the actual Au loadings (wt%), and AuZr for Au/ ZrO_2 .

2.2. Catalyst characterization

Before the characterization, the catalysts were reduced at 300 °C in 50 vol% H_2/N_2 for 2 h with a total flow rate of 13 ml min⁻¹. The Au and Na contents were determined by inductively coupled plasma optical emission spectroscopy (ICP-OES) using a 715-ES ICP emissions spectrometer (Varian, Palo Alto, CA, USA) after subjecting the samples to a microwave-assisted digestion process in a mixture of HF and aqua regia at 200 °C and 60 bar.

Surface area measurements were performed on a Micromeritics ASAP 2010 device. Prior to N_2 adsorption, 150 mg of the reduced catalyst were placed in the analysis tube and outgassed at 200 °C for 4 h. BET surface area and pore volume were calculated from N_2 adsorption isotherms measured at -196 °C. The average pore diameters were calculated from the desorption branch of the isotherm using the BJH method.

XRD patterns were recorded using a PANalytical X'Pert PRO diffractometer equipped with a X'Celerator RTMS detector using Ni-filtered $\text{Cu-K}\alpha$ radiation (1.54 Å) at 40 kV and 40 mA. Samples were mounted on silicon zero background holders, and the data were acquired stepwise (0.021°/s) between 5–100° with a divergence slit of 2°. Peak positions and profiles were fitted with a Pseudo-Voigt function using the HighScore Plus software package (Panalytical). Phase identification was done using the PDF-2 database of the International Center of Diffraction Data (ICDD).

X-ray Photoelectron spectroscopy (XPS) were recorded on an ESCALAB 220iXL (Thermo Fisher Scientific) with monochromated Al $\text{K}\alpha$ radiation ($E = 1486.6$ eV). Samples deposited on a stainless-steel holder with conductive double-sided adhesive carbon tape. The measurements were performed with charge compensation using a flood electron system combining low energy electrons and Ar^+ ions ($p_{\text{Ar}} = 1 \times 10^{-7}$ mbar). The electron binding energies are referenced to the C 1s core level of carbon at 284.8 eV (C-C and C-H bonds). For quantitative analysis, the peaks were deconvoluted with Gaussian-Lorentzian curves using the software Unifit 2023. The peak areas were normalized by the transmission function of the spectrometer and the element specific sensitivity factor of Scofield [27].

Scanning transmission electron microscopy (STEM) measurements were performed with an aberration-corrected JEM-ARM200F (Jeol, Corrector: CEOS) at 200 kV. A High-Angle Annular Dark Field (HAADF) and an Annular Bright Field (ABF) detector were used for STEM imaging. The catalysts were deposited without further treatment onto a copper grid with holey carbon support (mesh 300), which was then transferred to the microscope.

Transient study of D_2 interactions with 0.75AuZr, 0.04AuZr and ZrO_2 was performed in the temporal analysis of the products (TAP) reactor (TAP-2 system), as previously described in detail [28–30]. In these experiments, each catalyst (50 mg, fraction: 310–750 μm) was loaded in a home-made quartz-tube reactor within its isothermal zone and fixed between two layers of quartz particles (fraction: 250–355 μm). Before pulse experiments, the catalyst was treated in a flow of 50% H_2/Ar (6 ml min⁻¹) at 300 °C for 2 h. After the treatment the reactor was evacuated to ca. 10^{-5} Pa.

Transient experiments were performed at 300 °C in a single pulse mode using a $\text{D}_2/\text{Ar} = 1:1$ mixture. The total pulse size was $8.3\text{--}9.8 \times 10^{15}$ molecules. D_2 (Aldrich, 99.8 atom.% D) and Ar (Air Liquide, 5.0) were applied for preparing the mixture without additional purification. The gas composition at the reactor outlet was quantitatively analyzed by a quadrupole mass spectrometer (HAL RC 301 Hiden Analytical) at m/z signals of 4 (D_2), 3(HD) and 40 (Ar). Pulses for each m/z were repeated 10 times and averaged to improve the signal-to-noise ratio. The concentrations of D_2 and HD were calculated from the ratio of

the area of signal recorded at the respective m/z value to the area of Ar signal used as an inert standard. The fragmentation patterns and sensitivity factors required for these calculations were determined separately upon pulsing the same mixture in the reactor filled only with quartz particles.

2.3. In-situ DRIFTS measurements

In-situ DRIFT spectra were obtained using a Nicolet iS10 (Thermo Fischer Scientific) FTIR spectrometer using a standard high-temperature Praying Mantis reaction cell (Harrick) with CaF_2 windows equipped with a temperature control unit (Eurotherm) and connected to a gas dosing system with mass-flow controllers (Bronkhorst). The spectra were recorded (averaged 64 scans) in the range of $4000\text{--}400\text{ cm}^{-1}$ at a resolution of 4 cm^{-1} . Ca. 25 mg of pure catalyst powder was deposited on top of a layer of 90 mg quartz within the sample cup. Before the reaction, a reductive pretreatment in a stream of 50 vol% H_2/He (13 ml min^{-1}) was performed for 2 h at $300\text{ }^\circ\text{C}$. Subsequently, the reaction cell was purged with He at 18 ml min^{-1} for 30 min to evacuate the H_2 . Afterward, the temperature was reduced to $250\text{ }^\circ\text{C}$, and, at this temperature, the cell pressure was increased to 3 bar under He flow using a back pressure regulator (Swagelok) mounted at the outlet of the Harrick cell. Once the desired pressure was reached the gas was switched to the reaction mixture with a H_2 : CO_2 ratio of 3:1 ($9.0\text{ ml min}^{-1}\text{ H}_2$, $3.0\text{ ml min}^{-1}\text{ CO}_2$, $6.0\text{ ml min}^{-1}\text{ He}$). After 90 min reaction at $300\text{ }^\circ\text{C}$, the temperature was increased to $350\text{ }^\circ\text{C}$. For each step, the reaction was followed for 90 min. The intensity of the signals is given on the $\log(1/R)$ scale, where R is the sample reflectance.

Series of DRIFT experiments at 300 and $350\text{ }^\circ\text{C}$ were also carried out to identify the active surface intermediates that are mechanistically relevant for the RWGS reactions. Prior to spectral acquisition, the catalyst was reduced in 50 vol% H_2 in He (18 ml min^{-1}) for 2 h at $300\text{ }^\circ\text{C}$, purged by He for 3 h at the same temperature, and then left under He flow for 10 h at RT to minimize residual adsorbed H_2 on Au species. Afterward, the temperature was increased to the desired value and the cell pressure was increased to 3 bar under He flow at this temperature. Once the desired pressure was reached the catalysts were exposed to 16.6 vol% CO_2 in He (18 ml min^{-1}) for 20 min before switching to 50 vol % H_2 in He (18 ml min^{-1}). After appropriate background correction, the curve fitting of the DRIFT spectra was performed using the Fityk program [31] and assuming a Voigt peak shape [32].

2.4. In-situ EPR measurements

In-situ EPR spectra were recorded with a Bruker ELEXSYS 500–10/12 spectrometer operating in X-band at a microwave frequency of 9.32 GHz, a microwave power of 10 mW, and a modulation frequency of 100 kHz. Typically, 100 mg catalyst was placed inside a quartz plug-flow reactor connected to a gas dosing unit equipped with mass flow controllers (Bronkhorst) at the inlet and a quadrupole mass spectrometer (Omnistar, Pfeiffer Vacuum GmbH) at the outlet for online product analysis. Effective g values were calculated by Eq. (1).

$$g = \frac{h\nu}{\beta B_0} \quad (1)$$

in which h is the Planck constant, ν is the microwave frequency, β is the Bohr magneton, and B_0 is the external magnetic field.

The catalysts were first reduced at $280\text{ }^\circ\text{C}$ for 2 h in 50 vol% H_2 in He at a flow rate of 13 ml min^{-1} . The temperature was then reduced to ca. $-173\text{ }^\circ\text{C}$ and the corresponding spectra of the reduced catalysts were recorded. The temperature was then raised to $280\text{ }^\circ\text{C}$ under He with a flow rate of 13 ml min^{-1} . When the desired temperature was reached, the gas was switched to the reaction mixture ($9.0\text{ ml min}^{-1}\text{ H}_2$, $3.0\text{ ml min}^{-1}\text{ CO}_2$, $6.0\text{ ml min}^{-1}\text{ He}$). At these conditions, spectra were recorded for 2 h at 1 bar. After this time, the temperature was cooled

down to ca. $-173\text{ }^\circ\text{C}$, and the corresponding spectra of the spent catalysts were recorded.

2.5. Catalytic activity measurements

Catalytic tests were performed on an in-house setup consisting of 51 continuous-flow fixed-bed stainless-steel tubular reactors operating in parallel. The measurements were performed at 3 bar at temperatures ranging from 250 to $350\text{ }^\circ\text{C}$. The catalysts were pressed, crushed, and sieved to $310\text{--}750\text{ }\mu\text{m}$. Typically, the reactor (i.d. 4 mm) was filled with catalyst and 800 mg of SiC was placed on top of each catalyst bed to ensure plug flow. The catalysts were then reduced *in-situ* at $300\text{ }^\circ\text{C}$ and 1 bar for 2 h by heating them from RT to $300\text{ }^\circ\text{C}$ at a heating rate of $5\text{ }^\circ\text{C min}^{-1}$ in 50 vol% H_2 in N_2 at a flow rate of 13 ml min^{-1} . After that the catalysts were cooled down to reaction temperature ($250\text{--}350\text{ }^\circ\text{C}$), then a mixture of $\text{CO}_2/\text{H}_2/\text{N}_2 = 1/3/2$ was fed evenly to the reactors at two different flow rates (7.26 ml min^{-1} and 17.42 ml min^{-1}). The reaction products and the feed components were detected using an on-line Agilent HP 7890 gas chromatograph equipped with flame ionization (FID) and thermal conductivity (TCD) detectors. FFAP and AL/M columns were connected to FID for analyzing hydrocarbons. CO_2 , CO , H_2 and N_2 were separated using HP Plot/Q and MolSieve 5 A columns connected to TCD. The conversion of CO_2 was calculated from the inlet and outlet molar flow rates, as shown in Eq. (2). The selectivity to CO , CH_4 and CH_3OH was calculated using Eq. (3). The rates of CO formation (r_{CO}) normalized by Au mass and total catalyst mass were calculated by Eqs. (4) and (5), respectively.

$$X_{\text{CO}_2} = \frac{F_{\text{CO}_2,\text{in}} - F_{\text{CO}_2,\text{out}}}{F_{\text{CO}_2,\text{in}}} \times 100\% \quad (2)$$

$$S_x = \frac{F_{x,\text{in}}}{F_{\text{CO}_2,\text{in}} - F_{\text{CO}_2,\text{out}}} \times 100\% \quad (3)$$

$$r_{\text{CO}} = \frac{X_{\text{CO}_2} \times S_{\text{CO}} \times F_{\text{CO}_2}}{10000 \times m_{\text{Au}}} \quad (4)$$

$$r_{\text{CO}} = \frac{X_{\text{CO}_2} \times S_{\text{CO}} \times F_{\text{CO}_2}}{10000 \times m_{\text{cat}}} \quad (5)$$

where X_{CO_2} is the CO_2 conversion (%), S_x is the selectivity to x product (%), where x is the molar fraction of CO , CH_4 , or CH_3OH , F is a molar flow rate of CO_2 or product (x), and m_{Au} and m_{cat} are the amount of Au in gram of catalyst and total catalyst mass, respectively.

3. Results and discussions

3.1. Catalysts characterization

ICP-OES was used to obtain the actual Au and Na contents of all catalysts, and the results are shown in Table S1. As shown in Table S1, the amount of Na in the Au catalysts is comparable ($\sim 0.06\text{ wt}\%$), while the amount of Na in ZrO_2 is much higher ($0.36\text{ wt}\%$). When the support was treated with water alone to mimic the procedure of Au deposition, the amount of Na decreased to the level present in the Au catalysts. This indicates that a small amount of Na ($0.08\text{ wt}\%$) strongly bound to bare ZrO_2 and cannot be eliminated. It is assumed that the retained Na species are bound to the surface of ZrO_2 through -O-Na linkages, as suggested by XPS (Fig. 1c) [26]. They are suggested to play an important role in enhancing RWGS activity, as discussed in the following sections of this paper. XRD patterns of Au catalysts and the bare support are shown in Fig. 1a. No crystalline Au phases were observed in any of the samples, indicating that Au species were highly dispersed on the surface of the support. The specific surface area (S_{BET}), average pore size (D_p), and total pore volume (V_p) of bare support and Au catalysts are also summarized in Table S1, and the isotherm plots and pore size distribution plots are shown in Figs. S1 (Supplementary Material). The Au catalysts

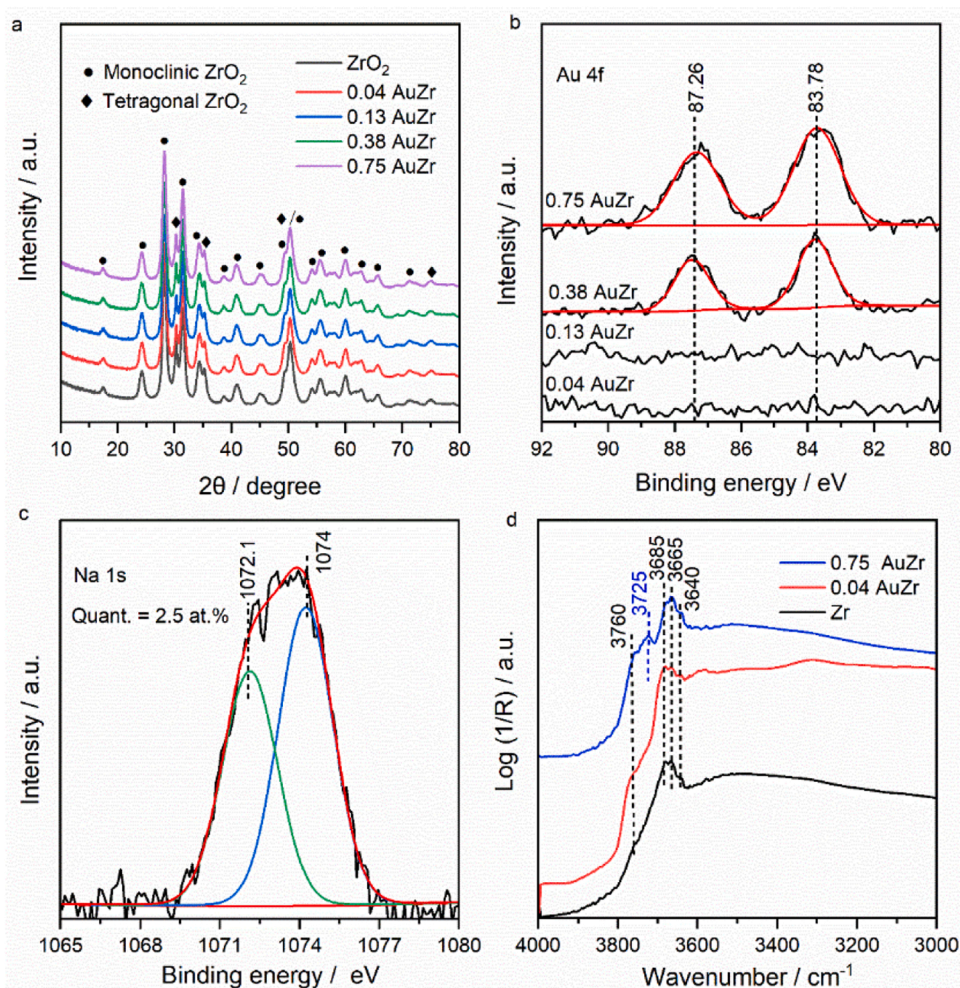


Fig. 1. (a) XRD powder patterns, (b) high-resolution XP spectra of Au 4f of supported Au catalysts, (c) high-resolution XP spectra of Na 1s of the bare ZrO₂ support, and (d) *in-situ* DRIFT spectra obtained in the OH stretching region for bare support (ZrO₂), 0.04 AuZr, and 0.75 AuZr catalysts after *in-situ* reduction at 300 °C in 50 vol% H₂/He for 2 h with a total flow rate of 13 ml min⁻¹.

showed values of S_{BET} , V_p , and average pore size (D_p) comparable to bare ZrO₂. XPS was used to characterize the bare support and Au catalysts. The Au 4f XP spectra of the Au catalysts are shown in Fig. 1b. No Au-related signals could be detected in samples with Au loadings ≤ 0.13 wt%. The Au 4f XP spectra of 0.34 AuZr and 0.75 AuZr catalysts show two peaks at 83.7 and 87.3 eV ascribed to Au 4f_{7/2} and Au 4f_{5/2}, respectively [11]. A distinct Na signal appears in the Na 1s XP spectrum of bare ZrO₂ (Fig. 1c). It can be deconvoluted into two distinct peaks at 1072.1 eV and 1074 eV. The former peak corresponds to -O-Na linkages, aligning with the typical Na 1s region in Na₂O crystal and exchanged Na in zeolites [33,34]. Meanwhile, the signal at 1074 eV corresponds to Na bonding with carbon-containing (NaO_xC_y) species [33,34]. This retained amount of Na could account for the high pH value (pH=10.7) observed in the suspension of bare ZrO₂ in deionized water. A substantial amount of Na⁺, weakly bound to the surface, is released into the solution during Au loading and subsequent filtration, leading to Na⁺ levels below the detection limit of XPS (Fig. S2). The DRIFT spectra in the hydroxyl regions on the catalysts after the reduction step. The IR spectrum of bare ZrO₂ shows four bands at 3760, 3685, 3665, and 3640 cm⁻¹. The band at 3760 is assigned to terminal OH groups [35], while the other bands are assigned to multicentered OH [35]. The same bands appear on the 0.04 AuZr catalyst. Increasing the Au loading to 0.75 wt% results in the appearance of a new band at 3725 cm⁻¹, which is most likely due to bridged OH groups [36]. These results reveal that the precipitation of

ZrO₂ at high pH also diversifies the types of surface hydroxyl groups, leading to the genesis of hydroxylated Na-modified ZrO₂.

Aberration corrected STEM was used to probe the existence of gold NPs, clusters, and single-sites over two selected Au catalysts. Fig. 2a-d present representative HAADF-STEM images of the 0.04 AuZr catalyst. At higher magnification, single Au sites and subnanometer Au clusters can be clearly seen in the HAADF-STEM image. For clarity, some Au sites and clusters are indicated by orange and red arrows, respectively (Fig. 2b, c). However, despite our thorough searching, we only found one Au nanoparticle in total on 0.04 AuZr catalyst (Fig. 2d). As this is the case, we are unable to estimate the average particle size of the Au NPs. This also precludes any dispersion calculations based on STEM measurements. Fig. 2e-h show the representative HAADF-STEM images of the 0.75 AuZr catalyst. Au species exists mainly as small nanoparticles with an average particle size of 2–5 nm. In addition to that particle type there are clusters below 2 nm and probably singular Au sites attached to the support surface. Au clusters and a few Au single sites can also be seen at high magnification (Fig. 2f). In some regions, there seems to be a surface layer of Au (green arrow, Fig. 2g) on the support. This layer is highly mobile and merges with the nearby Au nanoparticles when exposed to radiation. This variety of Au species and their morphology precludes any attempt to particle size statistics as the smaller species would be strongly underestimated due to imaging physics of the method.

Early studies on ZrO₂ revealed that molecular hydrogen (or deuterium) can undergo either heterolytic or homolytic dissociation, followed

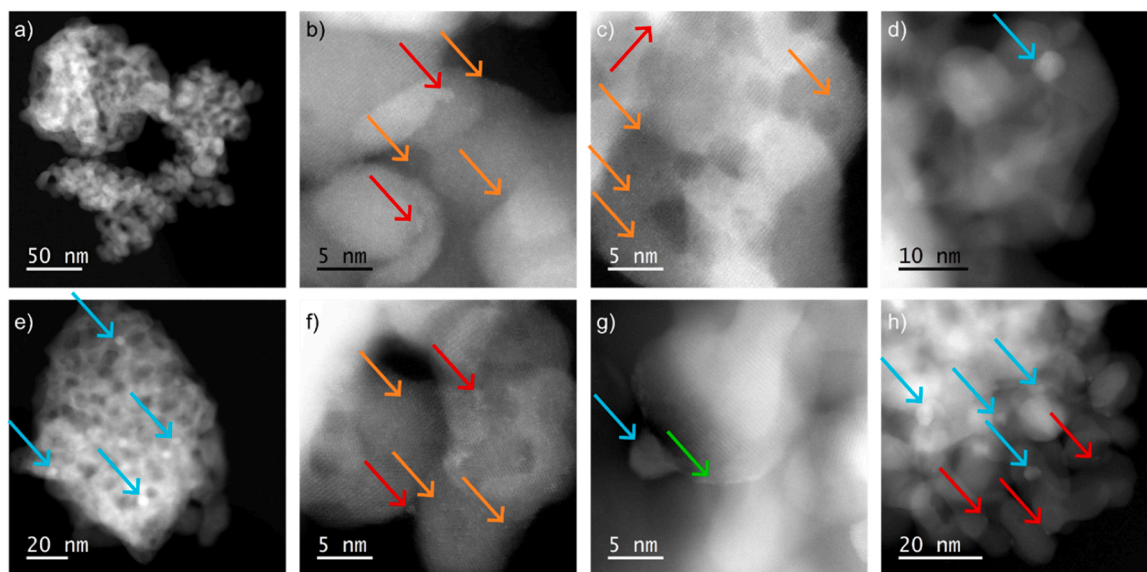


Fig. 2. HAADF-STEM images of the 0.04 AuZr (a-d), and 0.75AuZr (e-h) catalysts with Au NPs marked by blue arrows, clusters by red arrows, single sites by orange arrows, and surface coverings by green arrow.

by rapid diffusion across the oxide surface [37,38]. However, the presence of metal on the surface of ZrO_2 significantly enhanced the rate of H/D exchange of OH groups, owing to the greater ability of the metal to dissociate H_2 (D_2). Therefore, to explore the impact of Au on ZrO_2 activity in H/D exchange, we conducted a study in which D_2 was pulsed over reduced ZrO_2 , 0.04 AuZr and 0.75 AuZr at 300 °C using the TAP reactor. Our results revealed the presence of HD over all the tested materials (Fig. S3). As seen in Fig. 3, the amount of HD produced over bare ZrO_2 is only slightly lower than that over 0.04 AuZr but increases by around two times when 0.75AuZr was used as catalyst. Therefore, in agreement with literature data, Au loading favors deuterium dissociation and increases the amount of available D atoms which can spillover from supported Au species and interact with surface OH groups of ZrO_2 yielding HD.

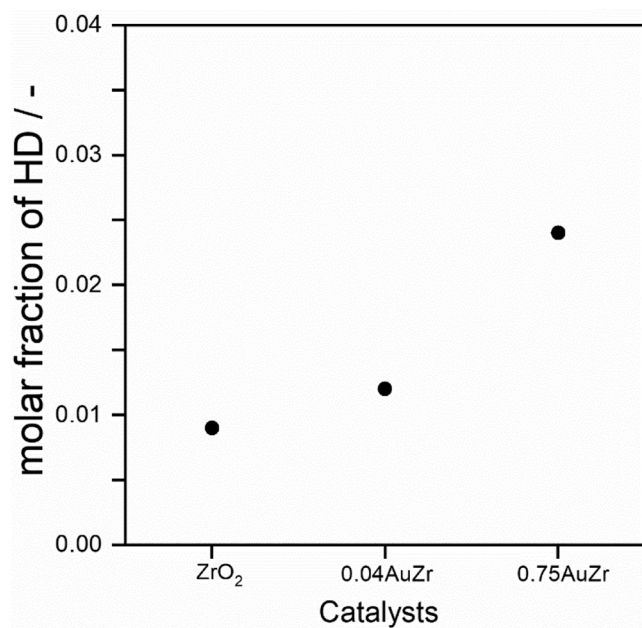


Fig. 3. Molar fraction of HD formed after single pulsing of D_2 :Ar = 1:1 mixture over the freshly reduced catalysts at 300 °C.

3.2. Catalytic performance evaluation

The catalytic performance of the bare zirconia (ZrO_2) and supported Au catalysts in the RWGS reaction was tested at temperatures ranging from 250 to 350 °C. After reductive pretreatment with H_2 at 300 °C for 2 h, the reaction was investigated at 3 bar in a fixed-bed continuous-flow reactor under a $\text{H}_2/\text{CO}_2/\text{N}_2$ mixture with a 3:1:2 molar ratio and a gas hourly space velocity (GHSV) of 4350, 8700, 10450 and 20903 $\text{ml g}_{\text{cat}}^{-1} \text{h}^{-1}$. Fig. 4a and S4a show the CO_2 conversion trends over the prepared catalysts as a function of temperature and Au loadings at GHSV of 10450 and 4350 $\text{ml g}_{\text{cat}}^{-1} \text{h}^{-1}$, respectively. The ZrO_2 support itself was poorly active with a CO_2 conversion of only 0.2% and 1.5% when the reaction temperature reached 350 °C at GHSV of 10450 and 4350 $\text{ml g}_{\text{cat}}^{-1} \text{h}^{-1}$, respectively. The CO_2 conversion significantly improved after loading Au. As expected, decreasing the space velocity (increasing residence time) leads to an increase in CO_2 conversion. The impact of Au loadings on CO selectivity is shown in Fig. 4b and S4b. The CO selectivity does almost not change over supported Au samples and remains above 98% throughout the test temperature range. Some catalysts, especially at low temperatures, produce a small amount of methanol (CH_3OH) alongside CO, with no formation of methane (CH_4). For instance, at 250 °C, the CO selectivity over 0.04 AuZr is 98.7%, with only 1.3% attributed to methanol. This modest methanol selectivity further decreases with increasing temperature, approaching almost 100% CO selectivity at 350 °C. It is worth noting that the decision to use an H_2/CO_2 ratio of 3 and a high pressure of 3 bar was made to illustrate that the catalysts exhibit a preference for the RWGS reaction even when the H_2/CO_2 ratio and pressure are high. It is well established that the hydrogenation of CO_2 under a hydrogen-rich atmosphere (with a higher H_2/CO_2 ratio) or high pressure promotes the further hydrogenation of the produced CO into methane or methanol [11], posing a challenge to achieving high CO selectivity under these conditions. However, in this study, the prepared catalysts demonstrated exceptional CO selectivity even under these conditions, suggesting that the catalysts lean towards the RWGS reaction rather than the pathways leading to methanol and methane.

The Au-mass-normalized and total catalyst mass-normalized CO formation rates measured at 300 °C are shown in Fig. 4c and Fig. S4c, respectively. It is worth noting that the rates of CO formation at high Au loadings (0.38 AuZr and 0.75AuZr) were measured at CO_2 conversions well below 10% (at high GHSV of 20903 $\text{ml g}_{\text{cat}}^{-1} \text{h}^{-1}$). As clearly shown

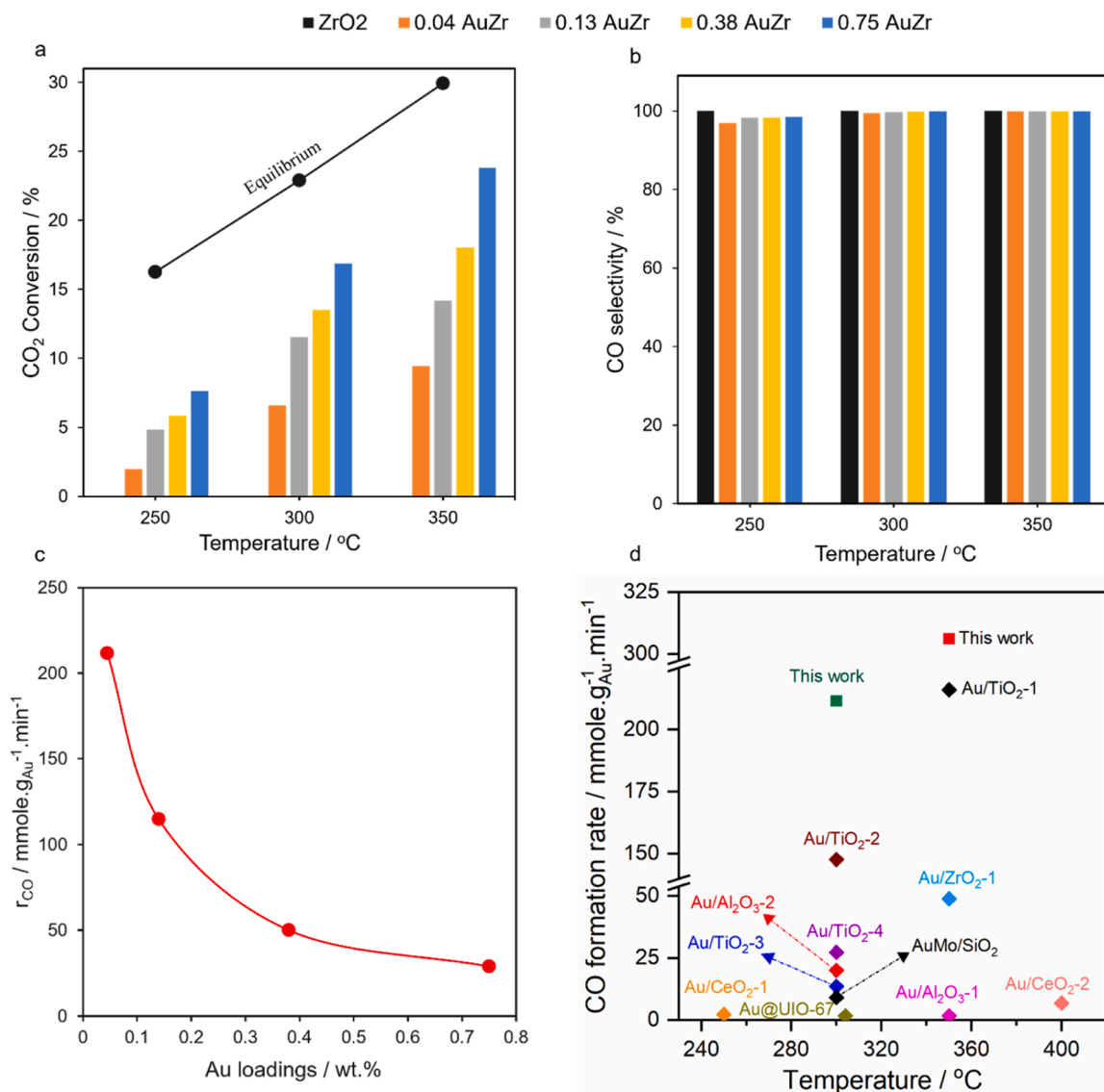


Fig. 4. (a) CO₂ conversion, (b) CO selectivity over the bare support (ZrO₂) and supported Au catalysts (xAuZr, x = 0.04, 0.13, 0.38, and 0.75 wt%-Au) as a function of reaction temperature (Reaction conditions: P_{total} = 3 bar, CO₂: H₂: N₂ = 1:3:2, GHSV = 10450 ml g_{cat}⁻¹ h⁻¹), (c) Au-mass normalized CO formation rate (Reaction conditions: P_{total} = 3 bar, CO₂: H₂: N₂ = 1:3:2, GHSV = 10450 and 20903 ml g_{cat}⁻¹ h⁻¹, and T = 300 °C), and (d) RWGS catalytic activity in terms of Au-mass normalized CO formation rate of 0.04 AuZr in comparison to Au-based catalysts reported in literature (Table S2).

in Fig. S5, the rates of CO formation at GHSV of 20903 ml g_{cat}⁻¹ h⁻¹ are more or less the same to that obtained at 10450 ml g_{cat}⁻¹ h⁻¹, thus under differential reactor conditions. The Au-mass-normalized CO formation rate (Fig. 4c) over 0.04 AuZr containing mainly single Au sites/nanoclusters was about 7 times higher than that of 0.75 AuZr dominated by Au NPs. This can be attributed to the high dispersion of Au in form of single sites and clusters, while the total catalyst mass-normalized CO formation rate (Fig. S4c) rises with increasing Au loading. In both cases, the rate of CO formation reached a semi-plateau at higher Au loadings (≥ 0.38 wt%). The apparent activation energy (E_a), as shown in Fig. S4d, is 44 kJ/mol over 0.04 AuZr, while for catalysts with Au loadings ≥ 0.13 wt%, the values of E_a are more or less the same. This suggests that these catalysts (≥ 0.13 wt%) share common active sites. This is also consistent with the HAADF-STEM images, which revealed that over 0.04 AuZr, Au species are mainly dispersed as single sites, while at higher Au loadings, Au NPs dominate. The lower apparent activation energy at higher gold loading (≥ 0.13 wt%) could be due to the enhanced hydrogen activation (Fig. 3). As compared with other Au-metal-based RWGS catalysts (Fig. 4d and Table S2), our 0.04 AuZr catalyst is one

of the highest performing catalysts in terms of Au-related activity. The Au-mass-normalized CO formation rate over catalysts containing ZrO₂ prepared at high pH of 12 (this study) is 10 times higher than over that based on ZrO₂ prepared at low pH of 9 (Fig. S6).

3.3. In-situ DRIFTS measurements

The investigation of surface species formed during the catalytic reaction plays a critical role in the understanding of the reaction mechanism. Therefore, series of DRIFTS measurements were carried out under near reaction conditions. We first conducted a blank experiment in which the DRIFT cell was filled solely with pure quartz, and then the RWGS reaction was performed under conditions typically similar to those employed thereafter for gold catalysts. As illustrated in Fig. S7, the spectrum (depicted in black) revealed only gaseous CO₂ [39], with no detection of any other gaseous products (such as CO or CH₄) or adsorbed carbon-containing species, suggesting the inertness of quartz in the RWGS reaction. For this study, the bare support (ZrO₂) as well as catalysts with the lowest (0.04 AuZr) and highest (0.75 AuZr) Au loadings

were chosen. Because carbon dioxide is an acidic molecule, it adsorbs on basic surface sites such as basic hydroxyl groups (terminal, t-OH), coordinatively unsaturated (cus) O^{2-} centers, or acid-base pair sites (cus $Zr^{4+}-O^{2-}$). When CO_2 reacts with basic terminal OH, bicarbonates are formed. As long as these terminal OH groups are isolated, they form monodentate bicarbonates ($m-HCO_3^-$, [Scheme S1\(I\)](#)) [40], whereas when they are in close proximity to cus- Zr^{4+} (i.e., oxygen vacancies) [40–42], they form bidentate bicarbonates ($b-HCO_3^-$, [Scheme S1\(II\)](#)). Monodentate carbonate species ($m-CO_3^{2-}$, [Scheme S1\(III\)](#)) are formed when CO_2 reacts with cus O^{2-} centers of high basicity [14], while bidentate carbonates ($b-CO_3^{2-}$, [Scheme S1\(IV\)](#)) are formed when CO_2 reacts with cus $Zr^{4+}-O^{2-}$ acid-base pair sites [14,40,42,43]. In addition, polydentate carbonate species are formed when CO_2 reacts with closely spaced cus Zr^{4+} centers [14].

[Fig. S8](#) depicts the temporal evolution of adsorbed carbon-containing species on the bare support during CO_2 hydrogenation at 300 °C as a function of reaction time. The assignment of DRIFT bands observed in the present study is shown in [Table 1](#). The DRIFT spectra exhibited several bands at 1690, 1630, 1420, 1335, 1290 and 1250 cm^{-1} . According to the literature [44–46], we attribute the bands at 1625 and 1420 cm^{-1} to $b-HCO_3^-$. The assignment of the band 1690, 1335, 1290 and 1250 cm^{-1} is ambiguous as it can be attributed to either $m-HCO_3^-$ or carboxylate-like ($CO_2^{\delta-}$) species, given that the positions of these surface species are typically similar ([Table 1](#)). Several studies have attributed the spectral band within the 1653–1705 cm^{-1} range to the $\nu_{as}(CO_3)$ modes of $m-HCO_3^-$ [44,47]. On the other hand, the formation of carboxylate species necessitates electron transfer from the surface to CO_2 , which in turn requires a negatively charged surface [48]. Several studies have reported that the addition of alkali cations, such as Li^+ and Na^+ , enhances the charge density on the surface [49–53]. This enhanced charge density could facilitate the formation of stabilized carboxylate-like species. Consequently, further *in-situ* DRIFT experiments were conducted to properly assign these bands (1690, 1335, 1290 and 1250 cm^{-1}) and to determine whether the presence of Na ions plays a role in the formation of these species. [Fig. S9](#) compares the DRIFT spectra of Na-free ZrO_2 prepared using NH_4OH at pH = 12 after exposure to CO_2 at 300 °C, in comparison with that prepared at the same pH using NaOH.

The DRIFT spectrum of Na-free ZrO_2 exhibits three main bands, corresponding to the typical IR bands of $b-HCO_3^-$ at 1630, 1420, and 1223 cm^{-1} , representing the $\nu_{as}(CO_3)$, $\nu_s(CO_3)$, and $\delta(HO)$ modes, respectively [44–46]. Additionally, there are weak bands at 1690 and 1335 cm^{-1} . This suggests that the bands at 1290 and 1250 cm^{-1} , along

with the notable increase in the intensity of bands at 1690 and 1335 cm^{-1} in the DRIFT spectrum of ZrO_2 prepared with NaOH at a high pH of 12, strongly indicate that these bands are most likely associated with Na ions. Previous studies have attributed the bands appearing within the range of 1326–1346 cm^{-1} to the asymmetric $\nu C=O$ vibration of bicarbonate anion species [54,55]. Therefore, the bands at 1690, 1290, and 1250 cm^{-1} could potentially be attributed to Na-stabilized carboxylate-like species. To further assist in assigning these bands, the ZrO_2 prepared at a high pH of 12 using NaOH was stirred for 3 h in distilled H_2O , filtered, thoroughly washed with distilled water, and then dried at 150 °C overnight. [Fig. S10](#) depicts the DRIFT spectrum of adsorbed CO_2 on washed ZrO_2 , in comparison with the spectrum of the as-synthesized ZrO_2 . As expected, following the washing process, the spectrum demonstrates a notable decrease in the intensity of bands at 1690, 1290, and 1250 cm^{-1} . This is in line with the ICP results ([Table S1](#)), which indicated a reduction in the Na content, along with a minor amount of Na ions still detectable on the washed ZrO_2 . Based on these results, it is thus more plausible to attribute these bands to Na-stabilized carboxylate-like species rather than $m-HCO_3^-$. The substantial formation of carboxylate-like species on ZrO_2 prepared at high pH of ~12 (aged for 24 h in the mother liquor), as described in this study ([Fig. S11](#)), can directly account for the increased activity observed in contrast to Au/ ZrO_2 prepared at a pH of 9 in our prior study, where carboxylate species were absent [11].

The DRIFT spectra ([Fig. 5a](#)) of 0.04 AuZr were also recorded under identical pre-treatment and reaction conditions as in the case of bare ZrO_2 . In addition to bicarbonate and carboxylate species present on the surface of the latter material, further DRIFT bands were observed in the spectra of 0.04 AuZr, which correspond to adsorbed bidentate formate ($b-HCOO^-$, 1590, 1387, and 1356 cm^{-1}) [56,57] and monodentate carbonate ($m-CO_3^{2-}$, 1525, 1475 cm^{-1}) species [37,43]. Despite both bare ZrO_2 and 0.04AuZr demonstrating similar capabilities in activating H_2 (D_2), as confirmed by TAP results ([Fig. 3](#)), they exhibit substantial differences in their efficiency in catalyzing carboxylate hydrogenation and subsequent dissociation into CO as concluded below from *in-situ* DRIFT spectra. These findings highlight the critical importance of the gold-support interface and H_2 spillover in achieving high RWGS performance.

To understand the role of Au particle size in the nature and reactivity of surface species, a similar DRIFT experiment was performed over 0.75 AuZr under identical reaction conditions, and the obtained DRIFT spectra are shown in [Fig. 5b](#). The DRIFTS results show that the adsorbed species (bicarbonates/carbonates as well as formates) detected on the surface of the two catalysts are the same, however, the band intensities and, thus, the relative abundance of carboxylate, bicarbonate and formate species are different. The spectra of 0.75 AuZr are dominated by bands of formate species ([Fig. 5b](#)). Carboxylate and bicarbonate species, however, dominate over formate species on 0.04 AuZr ([Fig. 5a](#)). The relatively low intensity of Carboxylate/bicarbonate species observed during RWGS on 0.75 AuZr could be explained by the rapid hydrogenation of these species on this catalyst. This is likely due to the presence of large Au NPs on the 0.75 AuZr catalyst. Wang et al. [58] reported similar observations when studying CO_2 hydrogenation over Pd/ Al_2O_3 , and they attributed the higher decomposition rate of bicarbonates over the catalyst with large Pd NPs to the high concentration of the involved active H-species. Moreover, [Fig. 5b](#) also shows the presence of bidentate carbonates species ($b-CO_3^{2-}$, 1560 cm^{-1}) on the surface of 0.75 AuZr that are not detected on the surface of 0.04 AuZr.

Additional DRIFT experiments were performed to identify the active surface intermediates that are mechanistically relevant to RWGS reactions. In these experiments we studied the formation of surface species after exposing the catalysts to CO_2 at 300 and 350 °C, and then we monitored the changes of the formed surface species after switching to H_2 gas.

[Fig. 6a](#) depicts DRIFT spectra of 0.04 AuZr during CO_2 exposure and subsequent switch to H_2 flow. Prior to spectral acquisition at 300 °C, the

Table 1

Vibrational Frequencies and assignments of the surface species formed on pure zirconia (Zr) and Au-supported catalysts.

assignment	vibration mode	wavenumber (cm^{-1})
Bidentate carbonate ($b-CO_3^{2-}$)	$\nu_{as}(OCO)$	1560-1580 [14,43,44]
Monodentate carbonate ($m-CO_3^{2-}$)	$\nu_{as}(OCO)$	1525 [43]
	$\nu_s(OCO)$	1465 [37]
	$\nu_{as}(OCO)$	1630 [43,44]
Bidentate bicarbonate ($b-HCO_3^-$)	$\nu_s(OCO)$	1326-1420 [44,54,55, 59]
	$\delta(COH)$	1225 [43,44]
	$\nu_{as}(OCO)$	1690-1700 [44,47,59]
	$\nu_s(OCO)$	1328-1340 [44,45]
	$\delta(COH)$	1225 [43,44,59]
Monodentate bicarbonate ($m-HCO_3^-$)	$\nu_{as}(OCO)$	1580-1590 [56,57]
	$\nu_s(OCO)$	1356 [56,57]
	$\delta(CH)$	1387 [56,57]
	$\nu(CH)$	2874 [57,60]
	$\delta(CH)$	2965 [57,61]
	$+ \nu_{as}(OCO)$	
	$\nu_{as}(OCO)$	1691-1700 [53,62]
Carboxyl COOH	$\nu_s(OCO)$	1250-1330 [53,62,63]
	$\nu_{as}(OCO)$	1510-1650 [62,64]
	$\nu_s(OCO)$	1280-1400 [62,64]

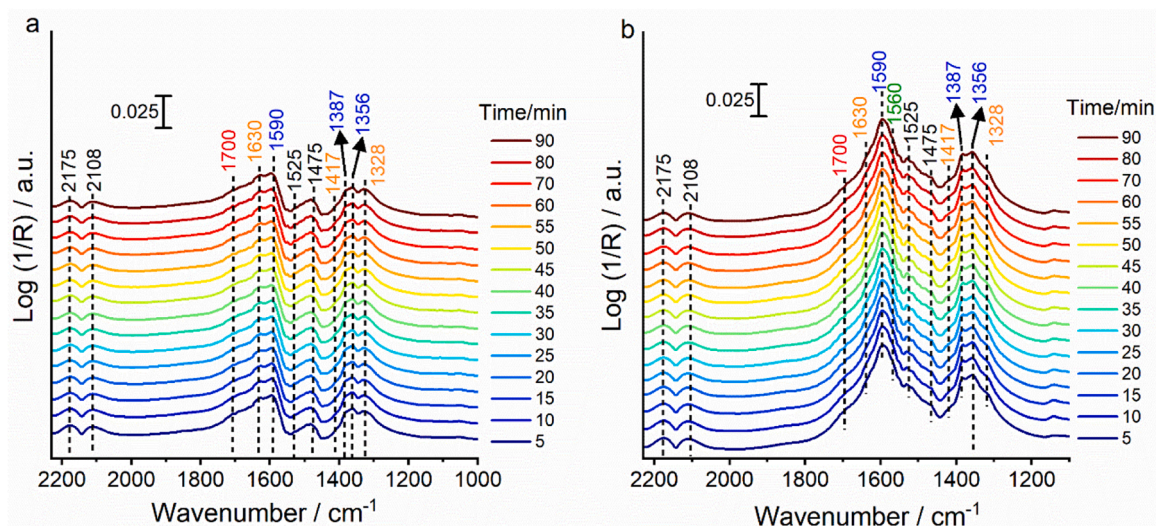


Fig. 5. Time-dependent *in-situ* DRIFT spectra of the RWGS reaction over (a) 0.04 AuZr and (b) 0.75 AuZr. Reaction conditions: P = 3 bar, T = 300 °C, H₂: CO₂: N₂ = 3:1:2; total flow rate = 18 ml.min⁻¹. The wavenumber values in red, orange, blue, green, and black colors represent the carboxylate, b-HCO₃⁻, b-HCOO⁻, b-CO₃²⁻ and m-CO₃²⁻ species, respectively.

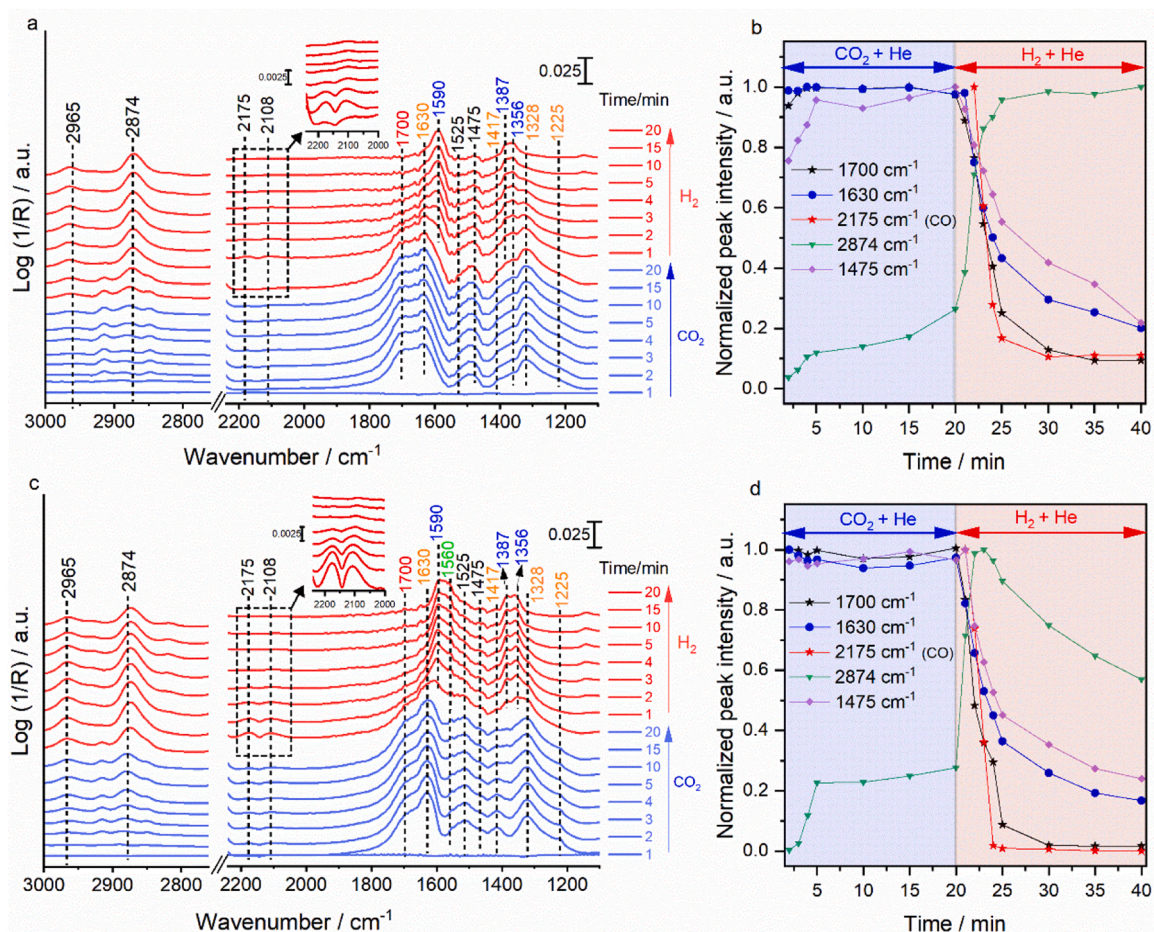


Fig. 6. Time-dependent *in-situ* DRIFT spectra obtained when the feed gas was switched between 16.6% CO₂ and 50% H₂ (both in He) at 300 °C under P = 3 bar and total flow rate = 18 ml min⁻¹ over (a) 0.04 AuZr and (c) 0.75 AuZr, and the corresponding evolution of normalized peak intensity of carboxylate/carboxyl-like (1700 cm⁻¹), b-HCO₃⁻ (1630 cm⁻¹), CO (2175 cm⁻¹), b-formate (2874 cm⁻¹), and m-CO₃²⁻ (1475 cm⁻¹) over b) 0.04 AuZr and d) 0.75 AuZr catalysts. The wavenumber values in red, orange, blue, green, and black colors represent the carboxylate, b-HCO₃⁻, b-HCOO⁻, b-CO₃²⁻ and m-CO₃²⁻ species, respectively.

catalyst was reduced in 50 vol% H₂ in He for 2 h at 300 °C, purged by He for 3 h at the same temperature (300 °C), and then left under He flow for 10 h at RT to ensure that all adsorbed H₂ on Au species was removed. The series of DRIFT spectra (blue spectra) collected during CO₂ exposure shows different DRIFT bands corresponding to various vibrational modes of adsorbed Carboxylate-like species (1700 cm⁻¹), b-HCO₃⁻ (1625, 1417, 1328 and 1225 cm⁻¹), and m-CO₃²⁻ (1525 and 1475 cm⁻¹). The band (at 1275 cm⁻¹) corresponding to $\nu_s(\text{OCO})$ of carboxylate-like species is clearly visible in the deconvoluted spectra presented in Fig. S12. It was noticed that very small bands in the range 2750–3000 cm⁻¹ appeared during CO₂ exposure, implying the formation of minute amounts of formate species, indicating the presence of residual adsorbed hydrogen even after extensive He purging.

The evolution of adsorbed Carboxylate, bicarbonates, monodentate carbonate, and bidentate formate species was followed by *in-situ* DRIFTS to get more information about the active intermediates responsible for CO formation. The intensity of the diagnostic peak for each species obtained through deconvolution of the DRIFTS spectra (Fig. S12) was normalized by its highest peak intensity and plotted as a function of time (Fig. 6b). When the feed gas was switched from CO₂ to H₂, the DRIFT intensities of Carboxylate-like species decreased rapidly, whereas the band intensities of b-HCO₃⁻ and m-CO₃²⁻ species decreased much slower. Concurrent with the disappearance of these species, the bands of gaseous CO (2145 cm⁻¹) became much stronger and new bands associated with bidentate formate (b-HCOO⁻) species began to emerge (1590, 1387, and 1356 cm⁻¹) (Fig. 6a). The CH bands of bidentate formate species in the range of 2700–3000 cm⁻¹ became also stronger (2965 and 2874 cm⁻¹). The b-HCOO⁻ (1590 cm⁻¹) species are very quickly accumulated on the surface and their intensity remained stable after 20 min of H₂ flow, and even when the temperature was raised to 350 °C in H₂ flow, formate species remained visible with appreciable

intensities (Fig. S13a). These findings indicate that b-HCOO⁻ species on the surface of 0.04 AuZr are spectators. The amount of gaseous CO decreased significantly after the vast majority of carboxylate-like species disappeared. These results provide direct evidence that the carboxylate-like species are the primary source of CO.

Similar experiments were carried out over 0.75 AuZr under identical conditions. The obtained DRIFT spectra and some of the deconvoluted spectra are shown in Fig. 6c and Fig. S14, respectively. When the catalyst is exposed to CO₂, CO₃²⁻, b-HCO₃⁻, m-CO₃²⁻, and b-CO₃²⁻ species are rapidly formed on the surface. Tiny amounts of formate (2874 and 2965 cm⁻¹), similar to 0.04 AuZr, are formed during CO₂ exposure due to the presence of residual adsorbed H species. When the feed gas was switched from CO₂ to H₂ at 300 °C, similar changes to those observed over 0.04 AuZr have been noticed in the DRIFT bands of CO₃²⁻, b-HCO₃⁻, and m-CO₃²⁻ species. The b-HCOO⁻ species (2874 and 2965 cm⁻¹), unlike those formed over 0.04 AuZr, began to decline very slowly after reaching their maximum (Fig. 6d). This can be attributed to the higher coverage of active H species, which is consistent with the results of H/D exchange transient experiments (Fig. 3). Remarkably, this indicates that at higher Au loadings, the b-HCOO⁻ species could also contribute to CO formation, though to a very low extent. Interestingly, it is evident from Figs. S15a that the intensity of the b-CO₃²⁻ species (1560 cm⁻¹) [14,43], which is not observed on 0.04 AuZr, gradually increases upon CO₂ exposure. Furthermore, its intensity is hardly affected by the H₂ flow, independent of whether the reaction temperature is 300 °C (Fig. S15a) or 350 °C (Fig. S13b). This suggests that these species are merely spectators. The enhanced formation of b-CO₃²⁻ species over 0.75 AuZr could be attributed to increased surface oxygen vacancy formation (Scheme S1 (IV)), as evidenced by *in-situ* EPR (*vide infra*, *in-situ* EPR Section 3.4). It is evident that the amount of adsorbed b-HCO₃⁻ on 0.75 AuZr is higher than that on 0.04 AuZr (Fig. S15b). This can also be attributed to the

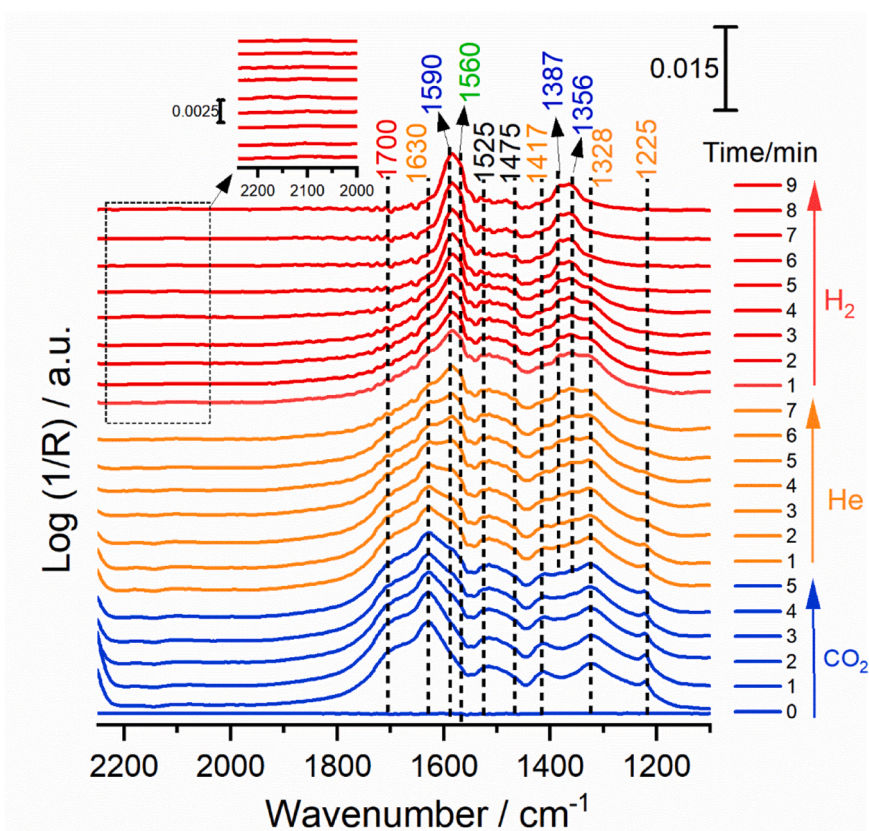


Fig. 7. Time-dependent *in-situ* DRIFT spectra obtained over 0.75 AuZr while switching the feed gas from 16.6% CO₂ (in He) to 100% He, followed by 50% H₂ (in He) at 300 °C under P = 3 bar and total flow rate = 18 ml min⁻¹. The wavenumber values in red, orange, blue, green, and black colors represent the carboxylate, b-HCO₃⁻, b-HCOO⁻, b-CO₃²⁻ and m-CO₃²⁻ species, respectively.

increased formation of oxygen vacancies on 0.75 AuZr. With a total increase in oxygen vacancies, there is also a higher probability that such vacancies are formed in close proximity to OH and cus-O^{2-} , which promotes the formation of bidentate bicarbonate (Scheme S1(II)) and carbonate species (Scheme S1(IV)), respectively. Collins et al. [41] have also come to a similar conclusion while investigating CO_2 adsorption over various gallium (III) oxide polymorphs.

Further *in-situ* DRIFTS experiments (Fig. 7) were conducted over 0.75 AuZr to investigate whether b-HCO_3^- and m-CO_3^{2-} species contribute to CO formation. These experiments followed a similar procedure as the ones shown in Fig. 6a and b, with the exception that He (orange spectra) was introduced between the CO_2 and H_2 gases for a specific duration. This step allowed the removal of the vast majority of the carboxylate-like species while still maintaining an appreciable amount of b-HCO_3^- and m-CO_3^{2-} . A negligible amount of CO was detected after feeding H_2 , suggesting that b-HCO_3^- and m-CO_3^{2-} species do not significantly contribute to CO formation. However, it is possible that they could be hydrogenated to b-HCOO^- species.

3.4. *In-situ* EPR measurements

EPR measurements were performed on the bare support and two selected samples of supported Au catalysts (0.04 AuZr and 0.75 AuZr) under near-reaction conditions (at 1 bar), to confirm the presence of oxygen vacancies (O_v) and uncover their role in the reaction mechanisms. The bare support and Au catalysts were first *in-situ* reduced at 280°C for 2 h under a flow of 50% H_2 in He. The EPR spectrum (Fig. S16) of the support material (ZrO_2) exhibits an isotropic signal at $g_{\text{iso}} = 2.003$, indicating the presence of oxygen vacancies with single trapped electrons [65,66]. Interestingly, the intensity of this signal further increased in the "spent form" after the CO_2/H_2 reaction. This can be explained by the prolonged exposure of the support material to hydrogen-rich reaction conditions (75% H_2) for additional 2 h. The EPR spectra (Fig. 8a and b) of the spent 0.04 AuZr and 0.75 AuZr catalysts show a new axial signal at $g_{\parallel} = 2.009$ and $g_{\perp} = 2.003$ (superimposed by the oxygen vacancy signal) which had previously been assigned to radicals containing carbon and oxygen [67]. Hence, the significant increase of the EPR signal in both spent catalysts (red lines in Fig. 8) might result not only from additional vacancies formed by prolonged exposure of the catalysts to hydrogen-rich reaction conditions (75% H_2) for additional 2 h but also from the overlap with the signal of the generated carbonate-based radicals.

The primary difference between the EPR spectra shown in Fig. 8a, b, and S16 is clearly visible in Fig. S17, where the intensity of the EPR signal of carbon and oxygen-containing radicals as well as of oxygen vacancies on 0.75 AuZr is higher than on 0.04 AuZr. DRIFTS studies revealed a higher abundance of b-HCO_3^- species on 0.75 AuZr compared to 0.04 AuZr (Fig. S15b), accompanied by the exclusive formation of b-CO_3^{2-} on 0.75 AuZr (Fig. 6c and S15a). Importantly, the formation of these species (b-HCO_3^- or b-CO_3^{2-}), as explained previously, relies on the presence of oxygen vacancies (as depicted in Scheme S1 (II) and (IV)). Therefore, the observed increase in the formation of these species on 0.75 AuZr aligns with the findings from EPR results and can be attributed to the enhanced generation of oxygen vacancies on this catalyst.

To identify the type of carbon and oxygen-containing radicals, we conducted a control experiment with identical conditions except that only a mixture of CO_2 and He was flowing without H_2 . The resulting EPR spectrum (not shown) displayed only the signal of oxygen vacancies. The signal of these radicals only appeared after the subsequent flow of H_2 or co-feeding of both CO_2 and H_2 simultaneously. Based on the findings from *in-situ* DRIFT spectra, these radicals could be tentatively attributed to b-HCOO^\bullet species, potentially formed through the hydrogenation of b-HCO_3^- by atomic hydrogen (H radicals). Similarly, it has been reported that the formate radical can be formed through the interaction of atomic hydrogen with carbon-containing species [68]. The formation of formate radical EPR signals on 0.04 AuZr and 0.75 AuZr can be attributed to the spill-over of hydrogen atoms from Au clusters and nanoparticles. Interestingly, this signal is absent on bare ZrO_2 , despite its comparable activity to 0.04 AuZr towards H_2 (D_2) as demonstrated in the TAP experiments. This may be due to the fact that H_2 undergoes predominantly heterolytic splitting on the acid-base pairs on the ZrO_2 surfaces [69]. This heterolytic dissociation of H_2 does not produce atomic H species, which are essential for the formation of formate radicals.

4. Possible reaction mechanisms

Both *in-situ* DRIFTS and TAP results clearly demonstrate that both the ZrO_2 support and the supported Au species (single sites, clusters, or NPs) play crucial roles in the activation of CO_2 and H_2 . The strong correlation between the decrease in the intensity of the 1700 cm^{-1} band and the release of CO provides compelling evidence that carboxylate-like species are indeed involved in the reaction mechanism. On the other hand, the b-HCO_3^- species at 1630 cm^{-1} is likely to be hydrogenated to formate (b-

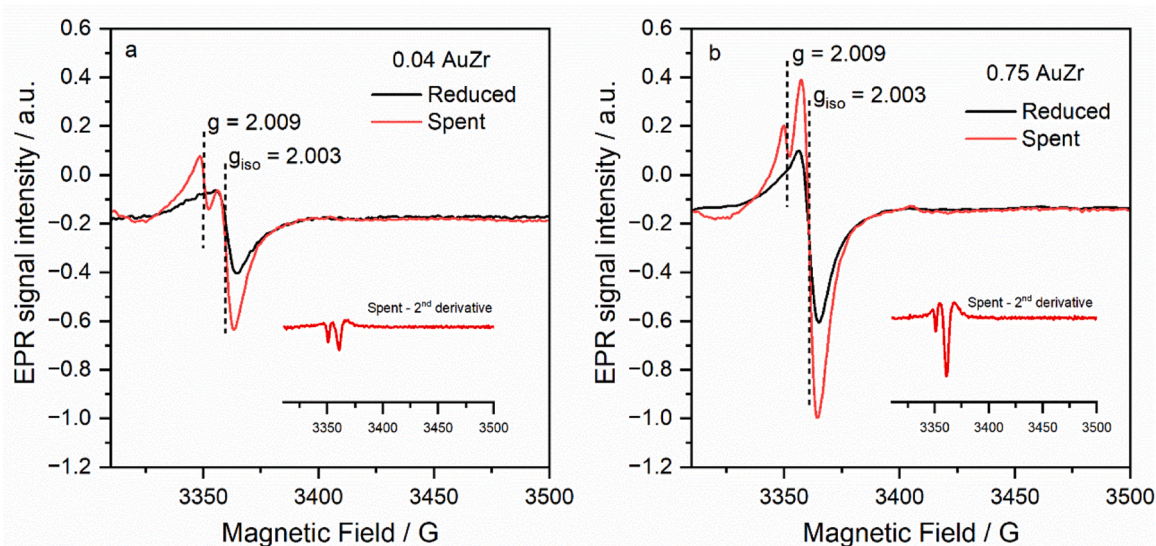


Fig. 8. *In-situ* EPR spectra obtained at -173°C for the reduced (at 280°C in 50% H_2/He for 2 h) and spent samples of (a) 0.04AuZr, and (b) 0.75 AuZr, Reaction conditions: $P = 1\text{ bar}$ H_2 : CO_2 : $\text{He} = 3:1:2$ total flow rate $= 18\text{ ml min}^{-1}$, $T = 280^\circ\text{C}$.

HCOO⁻ species, which is consistent with earlier studies [70]. Furthermore, the absence of CO formation over bare ZrO₂, despite the presence of H₂ activation and carboxylate-like species (1690 cm⁻¹), provides direct evidence for the pivotal role of H₂ spill-over and/or the gold-support interface in achieving high RWGS activity. These factors seem to significantly influence the destabilization of these active intermediates, thereby promoting their decomposition into CO.

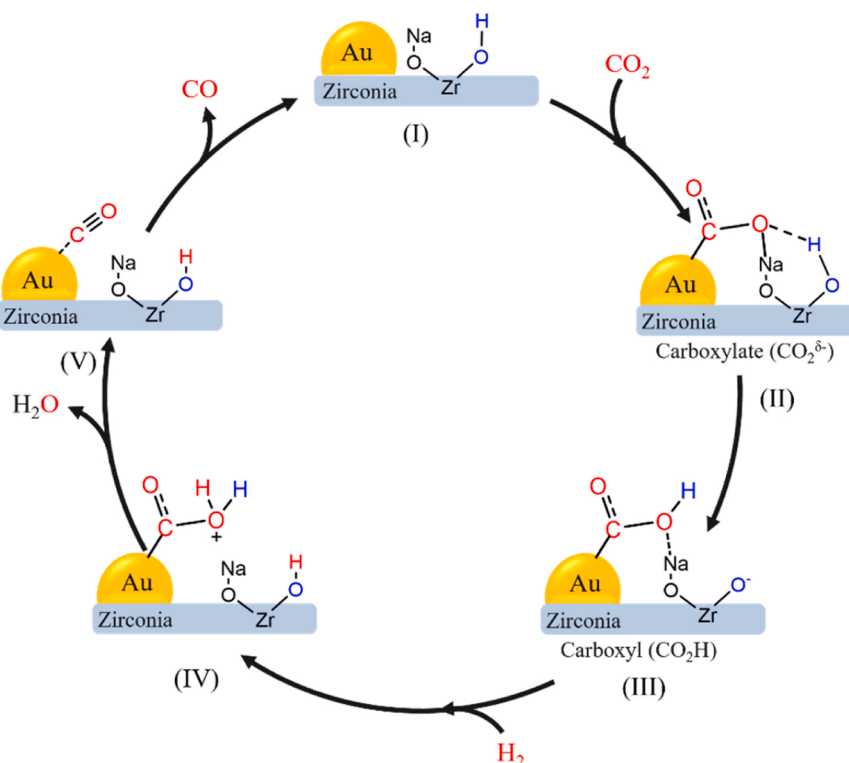
Additionally, *in-situ* DRIFTS results indicate that, at low Au loadings, the carboxylate-like species are the predominant active intermediates for CO formation, while the b-HCOO⁻ species mainly serve as spectators. However, at high Au loadings, in addition to the carboxylate pathway, part of the b-HCOO⁻ species could contribute, albeit to a very limited extent, to CO formation. DRIFTS studies also revealed that increasing the Au loading from 0.04 to 0.75 wt% leads to an increase in the number of b-HCO₃⁻ intermediate species (Fig. S15b) as well as to the formation of strongly adsorbed b-CO₃²⁻ species (spectators) (Fig. S15a and Scheme S1 (IV)) which were not detected on 0.04 AuZr. This is explained by the enhanced formation of oxygen vacancies at higher gold loading, as evidenced by *in-situ* EPR (Fig. 8b).

The DRIFTS results reveal the significant role of strongly adsorbed Na⁺ species in stabilizing and promoting the formation of carboxylate/carboxyl-like species. The bands associated with these species show notably low intensity in the absence of Na⁺ (Fig. S9) and are markedly reduced when the amount of Na is decreased (Fig. S10). The addition of alkali metals, such as K, to catalyst surfaces has been reported to stabilize adsorbed CO₂ through non-covalent bonds or electrostatic interactions between CO₂ and alkali metals.[50,51] Li et al.[53] demonstrated by DFT calculations that carboxylate species are stabilized on the surface of sodium-doped Rh/ZrO₂ in a tridentate geometry, with both oxygen atoms bound to Na ion and carbon bound to Zr⁴⁺. Similarly, the addition of Cs to Cu/ZnO significantly enhanced the binding strength of CO₂ to the surface, forming a C-Cu bond and a strong ionic-like O-Cs bond [71]. In noncatalytic systems, Floriani et al.[72,73] reported that the addition of alkali metals to low-valent Co complexes creates bifunctional systems that work cooperatively to activate CO₂ and

stabilize the transition metal-CO₂ adducts. Single-crystal X-ray diffraction analysis of the complex revealed that CO₂ is anchored in its intact form (i.e., as a carboxylate-like species) in a bent configuration to the low-valent cobalt ion via carbon, while the oxygen interacts with the alkali cation. Interestingly, the IR spectra of this complex exhibit bands at 1700–1680, 1275–1287, and 1208–1225 cm⁻¹ [73] which strongly resemble the IR bands in Figs. S12 and S14, indicating a similar type of CO₂ activation and the formation of similar species on our Au catalysts.

In two different studies by Flytzani-Stephanopoulos et al. [17,18], it was revealed that deposition of Au or Pt on alkali-promoted inert supports such as alumina or silica-based supports, stabilizes single-site Au or Pt in (Pt)Au-O(OH)_x-(Na or K) ensembles. These ensembles act as active sites for the low-temperature WGS reaction [17]. In their investigation, they reported an activation energy of 45 kJ/mol over gold on sodium-promoted KLTL-zeolite and MCM-41, with the carboxyl (COOH) species identified as the active intermediate [18]. Interestingly, this value aligns well with the apparent activation energy obtained from the Arrhenius plot over 0.04 AuZr (Fig. S4d), where the Au species are primarily dispersed as single sites. This suggests that our catalysts likely possess active sites of similar structure.

Based on the aforementioned results and discussion, we propose that the loading of Au on the Na-modified ZrO₂ support leads to the formation of Au/Na cooperative sites at the gold-support interface. These sites work synergistically to activate CO₂ and stabilize carboxylate species. Since the amount of Na remains relatively constant after loading Au on all Au catalysts (Table S1), increasing Au loading beyond a certain limit is expected to have a weaker impact on the reaction rate. This hypothesis finds support in Fig. 4c and S4c, where the reaction rate reaches a semi-plateau at Au loading ≥ 0.38 wt%. The primary reaction pathway over Au supported on Na-modified ZrO₂ can be described in the simplified Scheme 1. In this mechanism, CO₂ binds to the catalyst at the gold-support interface in a bent mode, with the electron-deficient carbon bound to Au, and one of the oxygens bound to Na⁺. The presence of nearby bridged or multicenter OH groups could serve as a local proton source, facilitating the protonation of the activated CO₂^{δ-} species into



Scheme 1. Summary of the possible steps in the carboxylate route for RWGS over Na modified ZrO₂ supported Au catalysts.

carboxyl-like (COOH) intermediates. This observation is consistent with DFT studies, which have demonstrated the crucial role of the hydroxylated surface in activating CO₂ and promoting the formation of carboxyl species (COOH) [74,75]. The formed -COOH species are further protonated before they finally decompose on the surface of the Au species into gaseous CO and H₂O. Protonation of carboxyl species is frequently considered as the rate-determining step in molecular catalysis [76]. This is because the proton sources required to protonate the OH of carboxyl species (step IV, Scheme 1) and hence weaken the C-OH should have a higher Brønsted acidity than those required to protonate carboxylate-like species (step III, Scheme 1). This is also consistent with lower activation energy values over catalysts with higher Au loadings (Fig. S4d), owing to the improved H₂ activation (Fig. 3). Additionally, although step V suggests that gold carbonyl species are formed, we did not observe any bands related to Au-CO bonded species in the *In-situ* DRIFT spectra within the studied temperature range. This is attributed to the weak adsorption between CO and Au species, as demonstrated in our previous study [11]. This weak interaction is also a plausible explanation for the observed superior CO selectivity.

5. Conclusion

We demonstrated that ZrO₂, prepared by precipitation at high pH and aged for 24 h in the mother liquor, leads to hydroxylated Na-modified ZrO₂, which is an excellent support for the preparation of highly active and selective Au catalysts for the RWGS reaction. The characterization results revealed that strongly adsorbed Na species are retained on the surface, most likely as surface -O-Na linkages. These Na species create, after adding Au, a cooperative Au/Na sites which play the crucial role in CO₂ activation and stabilization of the key reaction intermediate (carboxylate). The results also showed that single sites and clusters predominate at low Au loadings, and Au NPs at high Au loadings. At 300 °C, the CO formation rates on supported single Au sites/nanoclusters and Au NPs are $\sim 212 \text{ mmol.g}_{\text{Au}}^{-1}.\text{min}^{-1}$ respectively $\sim 29 \text{ mmol.g}_{\text{Au}}^{-1}.\text{min}^{-1}$, with > 98% CO selectivity. *In-situ* spectroscopic studies provided mechanistic insights into the reactivity of adsorbed surface species. The *in-situ* DRIFTS results show that carboxylate species are the primary source of gaseous CO. They also suggest that, at low Au loadings, carboxylates are the main active intermediates, while b-HCOO⁻ species are mostly spectators. At high Au loading, both carboxylates and a part of the b-HCOO⁻ species contribute to CO formation, likely due to a higher concentration of active H species, as evidenced by H/D exchange results. *In-situ* EPR confirmed oxygen vacancy formation, which increased significantly with increasing Au loading. According to the DRIFTS results, the higher concentration of oxygen vacancies at higher Au loadings enhances the formation of the stable b-HCOO⁻ species and promotes the generation of new b-CO₃²⁻ species strongly adsorbed on the surface which act as spectators.

Funding sources

Alexander von Humboldt Foundation (Bonn, Germany). European Commission through the H2020-MSCA-RISE-2020 and BIOALL project, Grant Agreement: 101008058.

Author contributions

The manuscript was written through contributions of all authors. All authors have given approval to the final version of the manuscript.

CRediT authorship contribution statement

Brückner Angelika: Methodology, Supervision, Validation, Writing – review & editing. **Rabeah Jabor:** Conceptualization, Methodology, Supervision, Validation, Writing – review & editing. **Rabee Abdallah I. M.:** Conceptualization, Formal analysis, Investigation, Methodology,

Writing – original draft. **Cisneros Sebastian:** Formal analysis, Investigation, Methodology, Data curation. **Zhao Dan:** Data curation, Formal analysis, Investigation, Methodology. **Kreyenschulte Carsten R.:** Data curation, Formal analysis, Investigation, Methodology. **Bartling Stephan:** Data curation, Formal analysis, Investigation, Methodology. **Kondratenko Vita:** Data curation, Formal analysis, Investigation, Methodology. **Kubis Christoph:** Formal analysis, Methodology. **Kondratenko Evgenii V.:** Methodology, Validation, Writing – review & editing.

Declaration of Competing Interest

The authors declare the following financial interests/personal relationships which may be considered as potential competing interests: Jabor Rabeah reports financial support was provided by H2020-MSCA-RISE-2020. Abdallah I. M. Rabee reports financial support was provided by Alexander von Humboldt Foundation. If there are other authors, they declare that they have no known competing financial interests or personal relationships that could have appeared to influence the work reported in this paper.

Data Availability

Data will be made available on request.

Acknowledgements

A.I.M.R. gratefully acknowledges the Alexander von Humboldt Foundation (Bonn, Germany) for a postdoctoral fellowship program and Minia University administration/Egypt for a leave of absence. Financial support from the European Commission through the H2020-MSCA-RISE-2020 BIOALL project (Grant Agreement: 101008058) is also acknowledged.

Appendix A. Supporting information

Supplementary data associated with this article can be found in the online version at doi:10.1016/j.apcatb.2023.123685.

References

- [1] W. Wang, S. Wang, X. Ma, J. Gong, Recent advances in catalytic hydrogenation of carbon dioxide, *Chem. Soc. Rev.* 40 (2011) 3703–3727.
- [2] M. González-Castaño, B. Dorneanu, H. Arellano-García, The reverse water gas shift reaction: a process systems engineering perspective, *React. Chem. Eng.* 6 (2021) 954–976.
- [3] B. Liu, Y. Wang, N. Huang, X. Lan, Z. Xie, J.G. Chen, T. Wang, Heterogeneous hydroformylation of alkenes by Rh-based catalysts, *Chem* 8 (2022) 2630–2658.
- [4] X. Chen, Y. Chen, C. Song, P. Ji, N. Wang, W. Wang, L. Cui, Recent advances in supported metal catalysts and oxide catalysts for the reverse water-gas shift reaction, *Front. Chem.* 8 (2020).
- [5] L.C. Grabow, A.A. Gokhale, S.T. Evans, J.A. Dumesic, M. Mavrikakis, Mechanism of the water gas shift reaction on Pt: first principles, experiments, and microkinetic modeling, *J. Phys. Chem. C* 112 (2008) 4608–4617.
- [6] A.A. Gokhale, J.A. Dumesic, M. Mavrikakis, On the mechanism of low-temperature water gas shift reaction on copper, *J. Am. Chem. Soc.* 130 (2008) 1402–1414.
- [7] N.C. Nelson, M.-T. Nguyen, V.-A. Glezakou, R. Rousseau, J. Szanyi, Carboxyl intermediate formation via an *in situ*-generated metastable active site during water-gas shift catalysis, *Nat. Catal.* 2 (2019) 916–924.
- [8] H. Sakurai, S. Tsubota, M. Haruta, Hydrogenation of CO₂ over gold supported on metal oxides, *Appl. Catal. A: Gen.* 102 (1993) 125–136.
- [9] V. Kyriakou, A. Vourros, I. Garagounis, S.A.C. Carabineiro, F.J. Maldonado-Hódar, G.E. Marnellos, M. Konsolakis, Highly active and stable TiO₂-supported Au nanoparticles for CO₂ reduction, *Catal. Commun.* 98 (2017) 52–56.
- [10] L.F. Bobadilla, J.L. Santos, S. Ivanova, J.A. Odriozola, A. Urakawa, Unravelling the role of oxygen vacancies in the mechanism of the reverse water–gas shift reaction by operando drifts and ultraviolet–visible spectroscopy, *ACS Catal.* 8 (2018) 7455–7467.
- [11] A.I.M. Rabee, D. Zhao, S. Cisneros, C.R. Kreyenschulte, V. Kondratenko, S. Bartling, C. Kubis, E.V. Kondratenko, A. Brückner, J. Rabeah, Role of interfacial oxygen vacancies in low-loaded Au-based catalysts for the low-temperature reverse water gas shift reaction, *Appl. Catal. B: Environ.* 321 (2023) 122083.

- [12] X. Zhu, X. Qu, X. Li, J. Liu, J. Liu, B. Zhu, C. Shi, Selective reduction of carbon dioxide to carbon monoxide over Au/CeO₂ catalyst and identification of reaction intermediate, *Chin. J. Catal.* 37 (2016) 2053–2058.
- [13] M. Ziemba, J. Weyel, C. Hess, Elucidating the mechanism of the reverse water–gas shift reaction over Au/CeO₂ catalysts using operando and transient spectroscopies, *Appl. Catal. B: Environ.* 301 (2022) 120825.
- [14] B. Bachiller-Baeza, I. Rodriguez-Ramos, A. Guerrero-Ruiz, Interaction of Carbon Dioxide with the Surface of Zirconia Polymorphs, *Langmuir* 14 (1998) 3556–3564.
- [15] K. Tanabe, Surface and catalytic properties of ZrO₂, *Mater. Chem. Phys.* 13 (1985) 347–364.
- [16] J.T. Kozlowski, R.J. Davis, Heterogeneous catalysts for the guerbet coupling of alcohols, *ACS Catal.* 3 (2013) 1588–1600.
- [17] Y. Zhai, D. Pierre, R. Si, W. Deng, P. Ferrin, A.U. Nilekar, G. Peng, J.A. Herron, D. C. Bell, H. Saltsburg, M. Mavrikakis, M. Flytzani-Stephanopoulos, Alkali-Stabilized Pt-OH_x species catalyze low-temperature water-gas shift reactions, *Science* 329 (2010) 1633–1636.
- [18] M. Yang, S. Li, Y. Wang, J.A. Herron, Y. Xu, L.F. Allard, S. Lee, J. Huang, M. Mavrikakis, M. Flytzani-Stephanopoulos, Catalytically active Au-O(OH)_x species stabilized by alkali ions on zeolites and mesoporous oxides, *Science* 346 (2014) 1498–1501.
- [19] J.R. Morse, M. Juneau, J.W. Baldwin, M.D. Porosoff, H.D. Willauer, Alkali promoted tungsten carbide as a selective catalyst for the reverse water gas shift reaction, *J. CO₂ Util.* 35 (2020) 38–46.
- [20] J.L. Santos, L.F. Bobadilla, M.A. Centeno, J.A. Odriozola, Operando DRIFTS-MS study of WGS and rWGS reaction on biochar-based Pt catalysts: the promotional effect of Na, *C. 4* (2018) 47.
- [21] X. Yang, X. Su, X. Chen, H. Duan, B. Liang, Q. Liu, X. Liu, Y. Ren, Y. Huang, T. Zhang, Promotion effects of potassium on the activity and selectivity of Pt/zeolite catalysts for reverse water gas shift reaction, *Appl. Catal. B: Environ.* 216 (2017) 95–105.
- [22] S. Navarro-Jaén, A. Szego, L.F. Bobadilla, Ó.H. Laguna, F. Romero-Sarria, M. A. Centeno, J.A. Odriozola, Operando spectroscopic evidence of the induced effect of residual species in the reaction intermediates during CO₂ hydrogenation over ruthenium nanoparticles, *ChemCatChem* 11 (2019) 2063–2068.
- [23] B.H. Davis, Effect of pH on crystal phase of ZrO₂ precipitated from solution and calcined at 600°C, *J. Am. Ceram. Soc.* 67 (1984) C-168–C-168.
- [24] G.A. Carter, M. Rowles, M.I. Ogden, R.D. Hart, C.E. Buckley, Industrial precipitation of zirconyl chloride: the effect of pH and solution concentration on calcination of zirconia, *Mater. Chem. Phys.* 116 (2009) 607–614.
- [25] A. Bortun, M. Bortun, J. Pardini, S.A. Khainakov, J.R. García, Synthesis and characterization of a mesoporous hydrous zirconium oxide used for arsenic removal from drinking water, *Mater. Res. Bull.* 45 (2010) 142–148.
- [26] C.B. Amphlett, L.A. McDonald, M.J. Redman, Synthetic inorganic ion-exchange materials—II: hydrous zirconium oxide and other oxides, *J. Inorg. Nucl. Chem.* 6 (1958) 236–245.
- [27] J.H. Scofield, Hartree-Slater subshell photoionization cross-sections at 1254 and 1487 eV, *J. Electron. Spectrosc. Relat. Phenom.* 8 (1976) 129–137.
- [28] K. Morgan, N. Maguire, R. Fushimi, J.T. Gleaves, A. Goguet, M.P. Harold, E. V. Kondratenko, U. Menon, Y. Schuurman, G.S. Yablonsky, Forty years of temporal analysis of products, *Catal. Sci. Technol.* 7 (2017) 2416–2439.
- [29] J.T. Gleaves, G.S. Yablonsky, P. Phanawadee, Y. Schuurman, TAP-2: an interrogative kinetics approach, *Appl. Catal. A: Gen.* 160 (1997) 55–88.
- [30] J. Pérez-Ramírez, E.V. Kondratenko, Evolution, achievements, and perspectives of the TAP technique, *Catal. Today* 121 (2007) 160–169.
- [31] M. Wojdyr, Fityk: a general-purpose peak fitting program, *J. Appl. Crystallogr.* 43 (2010) 1126–1128.
- [32] J.T. Reilly, J.M. Walsh, M.L. Greenfield, M.D. Donohue, Analysis of FT-IR spectroscopic data: The Voigt profile, *Spectrochim. Acta Part A: Mol. Spectrosc.* 48 (1992) 1459–1479.
- [33] M. Yang, J. Liu, S. Lee, B. Zugic, J. Huang, L.F. Allard, M. Flytzani-Stephanopoulos, A common single-Site Pt(II)–O(OH)_x species stabilized by sodium on “active” and “inert” supports catalyzes the water-gas shift reaction, *J. Am. Chem. Soc.* 137 (2015) 3470–3473.
- [34] J.F. Moulder, W.F. Stickle, P.E. Sobol, K.D. Bomben, in: J. Chastain (Ed.), *Handbook of X-ray photoelectron spectroscopy*, Perkin-Elmer Corp., Eden Prairie, 1992, pp. 50–51.
- [35] L.M. Kustov, V.B. Kazansky, F. Figueras, D. Tichit, Investigation of the acidic properties of ZrO₂ modified by SO₄²⁻ anions, *J. Catal.* 150 (1994) 143–149.
- [36] B. Azambre, L. Zenboudy, A. Koch, J.V. Weber, Adsorption and desorption of NO_x on commercial ceria-zirconia (Ce_{0.9}Zr_{0.1}O₂) mixed oxides: a combined TGA, TPD-MS, and DRIFTS study, *J. Phys. Chem. C* 113 (2009) 13287–13299.
- [37] K.-D. Jung, A.T. Bell, Role of hydrogen spillover in methanol synthesis over Cu/ZrO₂, *J. Catal.* 193 (2000) 207–223.
- [38] F. Ouyang, J.N. Kondo, K.-C. Maruya, K. Domen, Isotope-exchange reaction between hydrogen molecules and surface hydroxy groups on bare and modified ZrO₂, *J. Chem. Soc., Faraday Trans.* 92 (1996) 4491–4495.
- [39] S.M. Fehr, I. Krossing, Spectroscopic signatures of pressurized carbon dioxide in diffuse reflectance infrared spectroscopy of heterogeneous catalysts, *ChemCatChem* 12 (2020) 2622–2629.
- [40] B. Liu, C. Li, G. Zhang, X. Yao, S.S.C. Chuang, Z. Li, Oxygen vacancy promoting dimethyl carbonate synthesis from CO₂ and methanol over Zr-doped CeO₂ nanorods, *ACS Catal.* 8 (2018) 10446–10456.
- [41] S.E. Collins, M.A. Baltanás, A.L. Bonivardi, Infrared spectroscopic study of the carbon dioxide adsorption on the surface of Ga₂O₃ polymorphs, *J. Phys. Chem. B* 110 (2006) 5498–5507.
- [42] T. Akune, Y. Morita, S. Shirakawa, K. Katagiri, K. Inumaru, ZrO₂ nanocrystals as catalyst for synthesis of dimethylcarbonate from methanol and carbon dioxide: catalytic activity and elucidation of active sites, *Langmuir* 34 (2018) 23–29.
- [43] S. Kouvra, J. Andersin, K. Honkala, J. Lehtonen, L. Lefferts, J. Kanervo, Water and carbon oxides on monoclinic zirconia: experimental and computational insights, *Phys. Chem. Chem. Phys.* 16 (2014) 20650–20664.
- [44] I.M. Hill, S. Hanspal, Z.D. Young, R.J. Davis, DRIFTS of probe molecules adsorbed on magnesia, zirconia, and hydroxyapatite catalysts, *J. Phys. Chem. C* 119 (2015) 9186–9197.
- [45] D. Bianchi, T. Chafik, M. Khalfallah, S.J. Teichner, Intermediate species on zirconia supported methanol aerogel catalysts: IV. Adsorption of carbon dioxide, *Appl. Catal. A: Gen.* 112 (1994) 219–235.
- [46] K. Zhao, L. Wang, E. Moio, M. Calizzi, A. Züttel, Identifying reaction species by evolutionary fitting and kinetic analysis: an example of CO₂ hydrogenation in DRIFTS, *J. Phys. Chem. C* 123 (2019) 8785–8792.
- [47] K. Pokrovski, K.T. Jung, A.T. Bell, Investigation of CO and CO₂ Adsorption on Tetragonal and Monoclinic Zirconia, *Langmuir* 17 (2001) 4297–4303.
- [48] M.U. Khan, L. Wang, Z. Liu, Z. Gao, S. Wang, H. Li, W. Zhang, M. Wang, Z. Wang, C. Ma, J. Zeng, Pt₃Co Octapods as Superior Catalysts of CO₂ Hydrogenation, *Angew. Chem. Int. Ed.* 55 (2016) 9548–9552.
- [49] M. Gao, J. Zhang, P. Zhu, X. Liu, Z. Zheng, Unveiling the origin of alkali metal promotion in CO₂ methanation over Ru/ZrO₂, *Appl. Catal. B: Environ.* 314 (2022) 121476.
- [50] W. Liao, P. Liu, Methanol synthesis from CO₂ hydrogenation over a potassium-promoted Cu_xO/Cu(111) (x ≤ 2) model surface: rationalizing the potential of potassium in catalysis, *ACS Catal.* 10 (2020) 5723–5733.
- [51] Y. Matsumura, H. Hashimoto, H. Kobayashi, S. Yoshida, The role of sodium ions as adsorption sites in silicalite-1, *J. Chem. Soc., Faraday Trans.* 86 (1990) 561–565.
- [52] M.B. Ansari, S.-E. Park, Carbon dioxide utilization as a soft oxidant and promoter in catalysis, *Energy Environ. Sci.* 5 (2012) 9419–9437.
- [53] S. Li, Y. Xu, H. Wang, B. Teng, Q. Liu, Q. Li, L. Xu, X. Liu, J. Lu, Tuning the CO₂ hydrogenation selectivity of rhodium single-atom catalysts on zirconium dioxide with alkali ions, *Angew. Chem. Int. Ed.* 62 (2023) e202218167.
- [54] G. Busca, V. Lorenzelli, Infrared spectroscopic identification of species arising from reactive adsorption of carbon oxides on metal oxide surfaces, *Mater. Chem.* 7 (1982) 89–126.
- [55] D.L. Bernitt, K.O. Hartman, I.C. Hisatsune, Infrared spectra of isotopic bicarbonate monomer ions, *J. Chem. Phys.* 42 (2004) 3553–3558.
- [56] M.D. Rhodes, K.A. Pokrovski, A.T. Bell, The effects of zirconia morphology on methanol synthesis from CO and H₂ over Cu/ZrO₂ catalysts: part II. Transient-response infrared studies, *J. Catal.* 233 (2005) 210–220.
- [57] S. Kattel, B. Yan, Y. Yang, J.G. Chen, P. Liu, Optimizing binding energies of key intermediates for CO₂ hydrogenation to methanol over oxide-supported copper, *J. Am. Chem. Soc.* 138 (2016) 12440–12450.
- [58] X. Wang, H. Shi, J.H. Kwak, J. Szanyi, Mechanism of CO₂ hydrogenation on Pd/Al₂O₃ catalysts: kinetics and transient DRIFTS-MS studies, *ACS Catal.* 5 (2015) 6337–6349.
- [59] E.-M. Köck, M. Kogler, T. Biele, B. Klötzer, S. Penner, In situ FT-IR spectroscopic study of CO₂ and CO adsorption on Y₂O₃, ZrO₂, and yttria-stabilized ZrO₂, *J. Phys. Chem. C* 117 (2013) 17666–17673.
- [60] K.K. Bando, K. Sayama, H. Kusama, K. Okabe, H. Arakawa, In-situ FT-IR study on CO₂ hydrogenation over Cu catalysts supported on SiO₂, Al₂O₃, and TiO₂, *Appl. Catal. A: Gen.* 165 (1997) 391–409.
- [61] T. Tagawa, N. Nomura, M. Shimakage, S. Goto, Effect of supports on copper catalysts for methanol synthesis from CO₂ + H₂, *Res. Chem. Intermed.* 21 (1995) 193–202.
- [62] K.D. Dobson, A.J. McQuillan, In situ infrared spectroscopic analysis of the adsorption of aliphatic carboxylic acids to TiO₂, ZrO₂, Al₂O₃, and Ta₂O₅ from aqueous solutions, *Spectrochim. Acta Part A: Mol. Biomol. Spectrosc.* 55 (1999) 1395–1405.
- [63] I.V. Chernyshova, P. Somasundaran, S. Ponnuram, On the origin of the elusive first intermediate of CO₂ electroreduction, *Proc. Natl. Acad. Sci.* 115 (2018) E9261–E9270.
- [64] G. Ramis, G. Busca, V. Lorenzelli, Low-temperature CO₂ adsorption on metal oxides: spectroscopic characterization of some weakly adsorbed species, *Mater. Chem. Phys.* 29 (1991) 425–435.
- [65] C. Gionco, M.C. Paganini, E. Giamello, R. Burgess, C. Di Valentin, G. Pacchioni, Paramagnetic defects in polycrystalline zirconia: an EPR and DFT study, *Chem. Mater.* 25 (2013) 2243–2253.
- [66] S. Chen, A.M. Abdel-Mageed, M. Li, S. Cisneros, J. Bannmann, J. Rabeah, A. Brückner, A. Groß, R.J. Behm, Electronic metal-support interactions and their promotional effect on CO₂ methanation on Ru/ZrO₂ catalysts, *J. Catal.* 400 (2021) 407–420.
- [67] F. Callens, G. Vanhaelewyn, P. Matthys, E. Boesman, EPR of carbonate derived radicals: applications in dosimetry, dating and detection of irradiated food, *Appl. Magn. Reson.* 14 (1998) 235–254.
- [68] A. Álvarez, M. Borges, J.J. Corral-Pérez, J.G. Olcina, L. Hu, D. Cornu, R. Huang, D. Stoian, A. Urakawa, CO₂ activation over catalytic surfaces, *ChemPhysChem* 18 (2017) 3135–3141.
- [69] O. Syzgantseva, M. Calatayud, C. Minot, Hydrogen adsorption on monoclinic (1̄11) and (1̄01) ZrO₂ surfaces: a periodic ab initio study, *J. Phys. Chem. C* 114 (2010) 11918–11923.
- [70] X. Jia, X. Zhang, N. Rui, X. Hu, C.-J. Liu, Structural effect of Ni/ZrO₂ catalyst on CO₂ methanation with enhanced activity, *Appl. Catal. B: Environ.* 244 (2019) 159–169.

- [71] X. Wang, P.J. Ramírez, W. Liao, J.A. Rodriguez, P. Liu, Cesium-induced active sites for C–C coupling and ethanol synthesis from CO₂ hydrogenation on Cu/ZnO (0001 $\bar{1}$) surfaces, *J. Am. Chem. Soc.* 143 (2021) 13103–13112.
- [72] G. Fachinetti, C. Floriani, P.F. Zanazzi, Bifunctional activation of carbon dioxide. Synthesis and structure of a reversible carbon dioxide carrier, *J. Am. Chem. Soc.* 100 (1978) 7405–7407.
- [73] S. Gambarotta, F. Arena, C. Floriani, P.F. Zanazzi, Carbon dioxide fixation: bifunctional complexes containing acidic and basic sites working as reversible carriers, *J. Am. Chem. Soc.* 104 (1982) 5082–5092.
- [74] S. Yin, Q. Ge, Selective CO₂ hydrogenation on the γ -Al₂O₃ supported bimetallic Co–Cu catalyst, *Catal. Today* 194 (2012) 30–37.
- [75] Y.-x Pan, C.-j Liu, Q. Ge, Effect of surface hydroxyls on selective CO₂ hydrogenation over Ni₄/ γ -Al₂O₃: a density functional theory study, *J. Catal.* 272 (2010) 227–234.
- [76] R.N. Sampaio, B.N. DiMarco, J.J. Concepcion, Proton-coupled group transfer enables concerted protonation pathways relevant to small-molecule activation, *Inorg. Chem.* 60 (2021) 16953–16965.